3-D Printing, Characterizing and Evaluating the Mechanical Properties of 316L Stainless Steel Materials with Gradient Microstructure

Juanita P. Stephen

Thesis submitted to the faculty of the Virginia Polytechnic Institute and State University in partial fulfillment of the requirements for the degree of

Master of Science

In

Mechanical Engineering

Reza Mirzaeifar

Shivakumar Ranganathan

Pinar Acar

February 26th, 2021

Blacksburg, VA

Keywords: Selective Laser Melting, Material with Graded Microstructure, 316L Stainless Steel, Mechanical Properties, Equiaxial Cellular Structure, 3-D Printing, Laser Power, Scanning Speed, Hatch Spacing

Honeywell Federal Manufacturing and Technologies, LLC operates the Kansas City National Security Campus for the United Sates Department of Energy / National Nuclear Security Administration under contract number DE-NA0002839

3-D Printing, Characterizing and Evaluating the Mechanical Properties of 316L Stainless Steel Materials with Gradient Microstructure

Juanita P. Stephen

ABSTRACT

Making gradient in the microstructure of metals is proven to be a superior method for improving their mechanical properties. In this research, we 3D print, characterize and evaluate the mechanical properties of 316L Stainless Steel with a gradient in their microstructure. During 3D printing, the gradient in the microstructure is created by tailoring the processing parameters (hatch spacing, scanning speed, and laser power and scanning speed) of the Selective Laser Melting (SLM). The Materials with Graded Microstructure (MGMs) are characterized by optical and scanning electron microscopy (SEM). Image processing framework is utilized to reveal the distribution of cells and melt pools shapes and sizes in the volume of the material when the processing parameters change. It is shown that the laser power, scanning speed and the hatch spacing have a more significant effect on the size and shape of cells and melt pools compared to the speed. Multiple Dog bones are 3D printed with a microstructure that has smaller features (cells and melt polls) at the edges of the structure compared to the center. Tensile and fatigue tests are performed and compared for samples with constant and graded microstructures.

3-D Printing, Characterizing and Evaluating the Mechanical Properties of 316L Stainless Steel Materials with Gradient Microstructure

Juanita P. Stephen

GENERAL AUDIENCE ABSTRACT

The mechanical performance of Selective Laser Melting (SLM) fabricated materials is an important topic in research. Strengthening the performance of these materials can be achieved through implementing a gradient within the microstructure, referred to as Materials with Graded Microstructure (MGMs). A complicated microstructure can weaken the microstructure, and this can be resolved by optimizing the microstructure during SLM 3D printing, in which the processing parameters are tailored. In this study, the mechanical properties of these MGMs were characterized and evaluated. The gradient in these materials were created by modifying SLM process parameters (scanning speed, hatch spacing, and laser power and scanning speed) during the build. Optical and scanning electron microscopy (SEM) was used to characterize these the microstructure of these MGMs, and image processing was used to examine the distribution of cells and melt pools characteristics throughout the region where the processing parameters changed. This investigation shows that laser power, scanning speed, and hatch spacing have a direct effect on the size and shape of the cells and melt pools, compared to scanning speed, which shows an effect on melt pools. Dog bone structures are 3-D printed with a graded microstructure that has small cells and melt pools at the edges, compared to the center, by changing the laser power and scanning speed. Tensile and fatigue analysis are performed and compared for samples with constant and graded microstructures, which reveal that the mechanical properties of the MGMs perform similar to the parameter at the edges, but differently in fracture mechanics.

Acknowledgments

To Dr. Reza Mirzaeifar for his continued support and guidance in my research and course work. Thank you, Dr. Reza Mirzaiefar, for believing in me and pushing me to succeed. Your knowledge and willingness to assist me was greatly appreciated. Thank you to Dr. Pinar Acar and Dr. Shivakumar Ranganathan for serving on my committee.

Thank you to the New Horizons Graduate Scholars Program for giving me the opportunity to attend Virginia Tech and providing me with Teaching Assistantships that increased my knowledge of various Mechanical engineering topics.

Special gratitude for my peers at the Kansas City National Security Campus, who provided resources and continued knowledge to my research.

I want to thank the Future Materials Lab members who have contributed to the success of my courses, research, and professional development. Lastly, I would like to thank to my family and friends who supported and encouraged me throughout all my endeavors.

Table of Contents

List of Figures

List of Tables

List of Abbreviations

AM	Additive Manufacturing
SLM	Selective Laser Melting
MGM	Materials with Graded Microstructure
CAD	Computer-Aided Design
316L SS	316L Stainless Steel
PBF	Powder Bed Fusion
SEM	Scanning Electron Microscope
MPB	Melt Pool Boundary
3-D	Three Dimensional
EHT	Electron High Tension
EDM	Electrical Discharge Machining
UTS	Ultimate Tensile Strength
YS	Yield Strength
LCF	Low Cycle Fatigue

Chapter 1

1. Introduction

1.1 Powder Bed Fusion via Selective Laser Melting

Additive manufacturing (AM) is an emerging technology in the manufacturing industry that has increased productivity, decreased production time, and reduced production cost in the current market. It is currently being used in various industry subsectors, including aerospace, electronics, nuclear enterprise, and medical applications. The AM market grew by 28.6 percent between 2011 and 2012, increasing to $2.2 billion from $1.7 billion [1]. With the introduction of AM, the layer-by-layer build process was initially used for rapid prototyping and producing tools with specific geometries and has since evolved to being used for production-ready parts. The United States (US) manufacturing industry has advanced since the introduction of AM and has the most considerable funding for research and development (R&D). In the 2012 State of the Union Address, President Obama praised AM, stating that it has "the potential to revolutionize the way we make almost everything."

Traditional manufacturing processes include machining, joining, forming, and casting. AM is a method of joining due to its process of joining materials together to build objects. The AM process fabricates 3-D objects from computer-generated designs by depositing material layer-by-layer [1]. The capabilities of AM include the ability to construct complex geometries that conventional manufacturing processes could not produce. AM, or three-dimensional (3-D) printing, can be performed with numerous materials in different forms including, wires, powders, and resins. Various AM processes include sheet lamination, vat photopolymerization,

directed energy deposition, material jetting, material extrusion, powder bed fusion, and binder jetting [2]. One of these processes, Powder bed fusion (PBF), employs a chamber filled with powder that produced an object selectively using an energy source [2]. There are various PBF technologies, and a primary method is Selective Laser Melting (SLM). This AM technique melts metallic powders together using a high-power density laser [3]. This process deposits a thin layer of metallic powder melted regions based on a Computer-aided design (CAD). After one layer of the design is melted, the building platform is lowered, and another layer of powder is deposited. A re-coater then levels the new layer, and the laser melts the next layer of the spliced CAD design (*Figure 1.1*a).

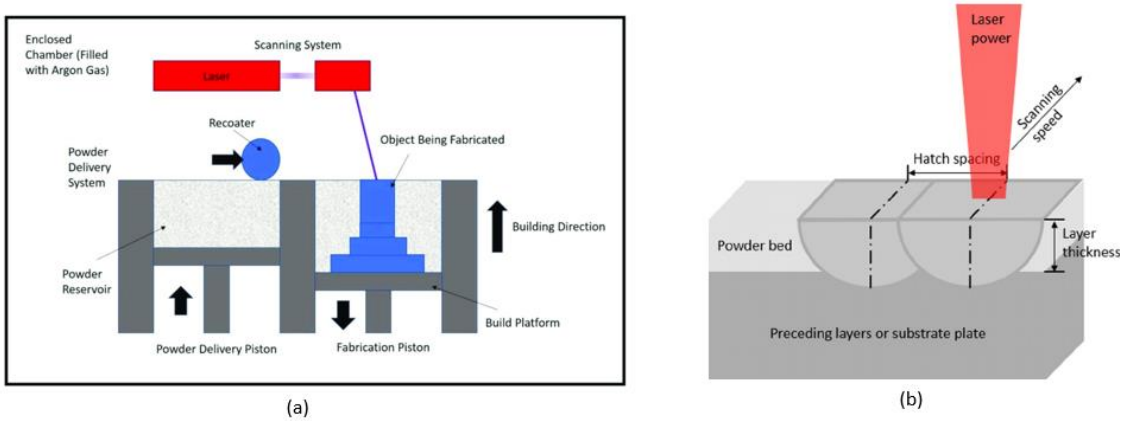

Figure 1.1(a) Selective Laser Melting process diagram [4]. (b) SLM Process Parameters [5] including hatch spacing, laser power, layer thickness, and scanning speed.

The laser beams can be directed and focused, allowing the powder to be selectively melted to form the part according to the CAD design. Within this process, various parameters can be changed to optimize different properties [4]. Some of the most common process parameters include laser power, hatch spacing, scanning speed, and layer thickness (Figure 1.1b). Characterizing the material from these printed objects is imperative to understand these AM processes' effect on the mechanical properties.

1.2 Materials with Graded Microstructure

Functionally graded materials (FGM) are materials in which there is a gradual change in either composition, microstructure, or porosity throughout the material [5]. The initial purpose of FGMs was to replace the existence of distinct interfacial regions in composite materials with a gradient interface. FGMs have since evolved to include the change in the chemical composition of the material at the interface. As interest in these materials grew, other FGMs have developed to include composition, microstructure, and porosity gradient materials.

Materials with Graded Microstructure (MGM) are designed to produce different microstructures throughout the material and occurs during the solidification process. This type of MGM has applications in the defense industry, where the material is made to attain the material's desired properties. Examples of these MGMs include bearings, shafts, or case-hardened steel [6]. There are different methods to achieve MGMs, including heat treatments and gradually changing process parameters during the build. Heat treatment is a process that involves heating and cooling a material in such a way to produce desired mechanical and microstructural properties. Heat treatment is the more conventional method for creating MGMs, however in this research, the microstructure formation will be controlled by changing the process parameters during the build.

1.3 Mechanical Testing

One of the most critical mechanical responses is the designed part's tensile behavior, per requirements and standards. The most prominent forms of mechanical testing are tensile and fatigue testing. The standard typically used for tensile test procedures and specimens is the ASTM E8/E8M – 13a, which was used as a basis for the tests conducted in this study. A tensile

test (Figure 1.2) observes mechanical properties by pulling the sample from either end typically until it breaks, and fatigue testing focuses on cyclic loading to analyze the fatigue life. Mechanical properties are physical properties of how the material performs when forces are applied. Due to higher cooling rates, the microstructure of SLM- fabricated parts is distinctive from conventionally manufactured parts [7]. The complicated microstructures in these metals and alloys diminish mechanical properties. There is a need to do extensive research studying the effect of possible modifications in microstructure as a direct result of processing parameters during SLM alloys' printing process to improve material properties.

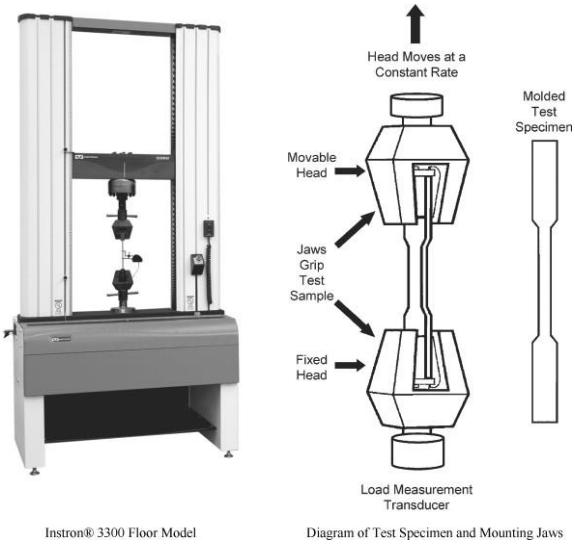

Figure 1.2 Tensile Machine schematic [6].

Due to the complexities of the SLM process, various research focuses on optimizing process parameters [8-11], to produce a uniform microstructure that provides acceptable mechanical properties. It has been reported that there is more deviation in elongation associated with the existence of unconsolidated powder particles within the structure [12]. Current work has focused on analyzing the effect of the process parameter being a particular variable that changes from part to part, rather than the variable changing throughout the part.

[8-11], In this work, the influence of gradient process parameters on the microstructure and mechanical properties of these 316L Stainless Steel SLM builds will be investigated. The following chapters will investigate the effect of changing a specific process parameter set during the build [13]. Chapter 2 examines cellular and melt pool characterization on gradient structures. In Chapter 3, a specific gradient process parameter is tested to observe the mechanical response.

Chapter 2

2. 3-D Printing and Characterizing Materials with Gradient Microstructure

2.1 Introduction

MGMs are formed during the solidification process. In SLM, multiple process parameters affect the formation of the microstructure, and some of these parameters will have a gradation during the build. Samples were printed via the SLM process to obtain stable parts with varying microstructure throughout a particular direction using 316L Stainless Steel powder [14]. The specimens were fabricated in a Renishaw AM250 machine with a Fiber YAG Gaussian circular beam and a powder size range between 15 and 45 microns. The chemical position of the 316L SS powder used for this build is shown in Table 2-1.

Table 2-1 Chemical composition in wt. % of AISI 316L powder [14].

C	**Si**	**Mn**	**P**	**S**	**N**	**Cr**	**Mo**	**Ni**	**Fe**
Max	Max	Max	Max	Max	Max	Min-Max	Min-Max	Min-Max	Balance
0.03	1.00	2.00	0.045	0.03	0.10	16.00-18.00	2.00-3.00	10.00-14.00	

Three sets of cube samples were printed, with dimensions of 10 by 10 by 12 millimeters, where 2 millimeters of the 12-millimeter dimension were cut off during the wire Electrical Discharge Machining (EDM) process of removing the specimens from the build plate. In the build process, specific process parameters were changed stepwise throughout the build direction to create a changing parameter gradation.

Under investigation, the process parameters include laser power, scanning speed, and hatch spacing due to their ability to be manipulated during the build [15]. During the parameter selection process, the current scope of work on optimizing specific parameters was considered [16-19]. The current optimized parameter for the machine was used as a basis for selecting the parameters as well.

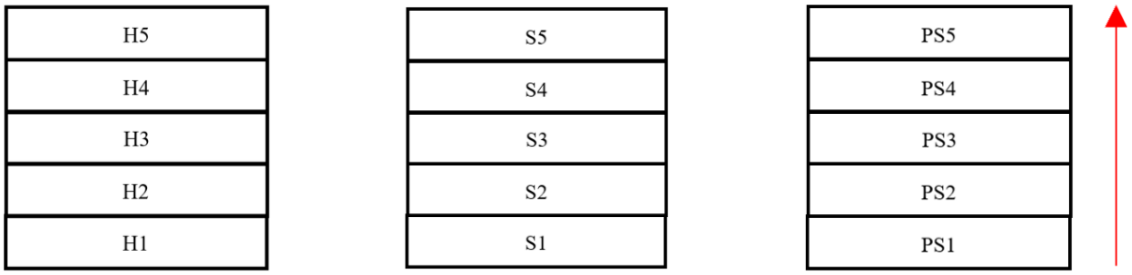

Figure 2.1 Block specimen printing, 10mm square block, with build direction.

For each set of parameters, a value was increased or decreased to create a gradient structure with five levels (*Figure 2.1*). The parameter changed every 2 millimeters as the part was built in the Z- direction. The parameters are labeled from one to five in the build direction. This build's layer thickness was set at a constant value of 50 microns and a beam spot size of approximately 70 microns. Typically, when the scanning speed or power is changed, the other parameter is changed as well. As a result of this effect, laser power and scanning speed were changed as a parameter set. This machine's current optimized variable includes a laser power of 200W, scanning speed of 0.75 m/s, and a hatch spacing of approximately 110 microns.

Table 2-2 Parameter designation and set for each level outlined in Figure 2.1.

Parameter Set	Power (W)	Speed (m/s)	Hatch Spacing (μm)
H1	200	0.75	75
H2	200	0.75	85
H3	200	0.75	95

H4	200	0.75	105
H5	200	0.75	115
S1	200	0.75	110
S2	200	0.70	110
S3	200	0.65	110
S4	200	0.60	110
S5	200	0.55	110
PS1	200	0.80	110
PS2	195	0.75	110
PS3	190	0.70	110
PS4	185	0.65	110
PS5	180	0.60	110

Hatch spacing is increased from 75 microns to 115 microns by 10 microns every 2 millimeters. Starting with the lower hatch spacing allows the build to have smaller melt pools, and as the hatch spacing increasing the melt pools will change in size and become more extensive. The next parameter is scanning speed, and it was decreased from 0.75 m/s to 0.55 m/s, where the optimized scanning speed is 0.75 m/s, and a constant laser power of 200W. The build began with the current optimized laser power and scanning speed, and the speed decreased. As the speed increased, the laser power is usually increased to account for energy applied to the powder during the build and ensure proper fusion. Due to the laser power and scanning speed typically having this effect on the microstructure, the last parameter set focused on changing the power and speed. The laser power was decreased from 200W to 180W, and the speed was decreased from 0.80 m/s to 0.60 m/s. These graded specimens were then analyzed according to the process outlined in Section 2.2.

2.2 Melt Pool and Cellular Characterization Methods

2.2.1 Specimen Preparation

Upon receipt of MGM specimens, each sample was dusted using compressed air and prepped for the characterization process. The build direction and sample orientation were determined before the epoxy setting to ensure the prepped surface would depict the melt pools formed during the build process. An epoxy mixture of resin to hardener, 100:12, by weight was created and poured into a 1-inch diameter cylinder mold over the specimens where the desired polished surface was lying face down. They were left under a vacuum for one hour and then placed in a vent hood for 24 hours to set. The specimens were removed from the mold to begin the grinding process using a METPREP 3 Polishing/Grinding System with grinding pads ranging from 240-1200 grit (Figure 2.2). Upon completion of grinding, polishing pads with 6µm and 0.05µm grit was used. A 6-micron pad was used for polishing with a Green Lube polishing lubricant and a glycol-based Polycrystalline Diamond Suspension lubricant periodically during the polishing. Lastly, the samples were polished using a 0.05-micron pad with a Colloidal Silica Suspension lubricant.

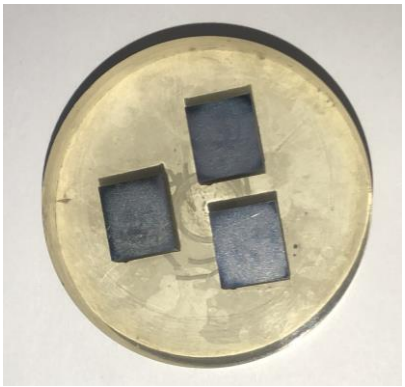

Figure 2.2 Image of Specimens inside of epoxy before final stages of polishing and etching.

Upon completion of grinding and polishing, the samples were etched, a process that reveals details in the microstructure that would not be as evident in as-polished images. Under a vent hood, the etching solution is composed of Nitric Acid, 6N, and Hydrochloric Acid, 6M with a ratio of 1 to 3, respectively. After the etchant was made, a plastic pipette is used to drop approximately 4-5 drops of the solution onto the samples' polished surface. The etchant is left on the sample for three and a half minutes and then rinsed and air-dried to then be imaged by an optical microscope. Polarized light improves image quality and allows objects to be seen that otherwise could not be seen typically [20]. Each block sample was prepared similarly for image analysis.

2.2.2 Optical and Scanning Electron Microscopy

Optical images were taken to capture the melt pools and grains in the structures. A melt pool is formed according to Figure 1.1 during the SLM process as the molten material that the laser beam has melted solidifies after each pass of the laser [21]. Similarly, the grain is formed during the solidification of the metal within and throughout the melt pools. Tiny crystals within the material begin to grow larger as the molten powder cools [22]. Grain growth can also be attributed to the heat treatment process, where the specimen is heated to a specific temperature to change characteristics and increase mechanical performance. While the molten powder on the previous layer cools, it is remelted as the laser crosses over the path, and epitaxial grain growth occurs at the melt pool boundary [23]. These grains grow in the maximum temperature gradient direction and follow the schematic shown in Figure 2.3.

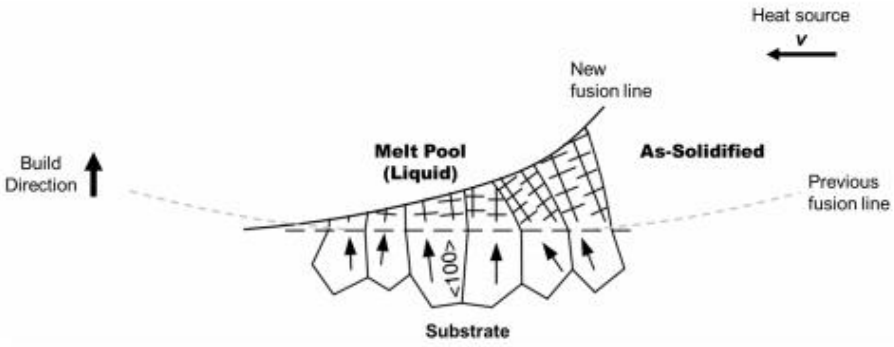

Figure 2.3 Schematic of epitaxial grain growth as the heat source moves away. The arrows signify the growth direction [23].

The melt pools were imaged under the optical microscope's polarized lens and used to analyze the sections to come. The optical images are shown below for each graded sample, where the melt pools and grains can be seen throughout. Each figure has an image of the entire length of the sample in the center with a scale bar of 1000 microns, and at specific locations, images were taken zoomed in with a scale of 100 microns. The image in the center was stitched using a function within the microscope program. Each image on either side of the full-length image shows a more detailed view of the melt pools and grains, resulting from the polarized lens's etching effect. Once the optical images were taken, each of these MGM specimens was taken to get images at a higher magnification scale to reveal the material's cellular shapes.

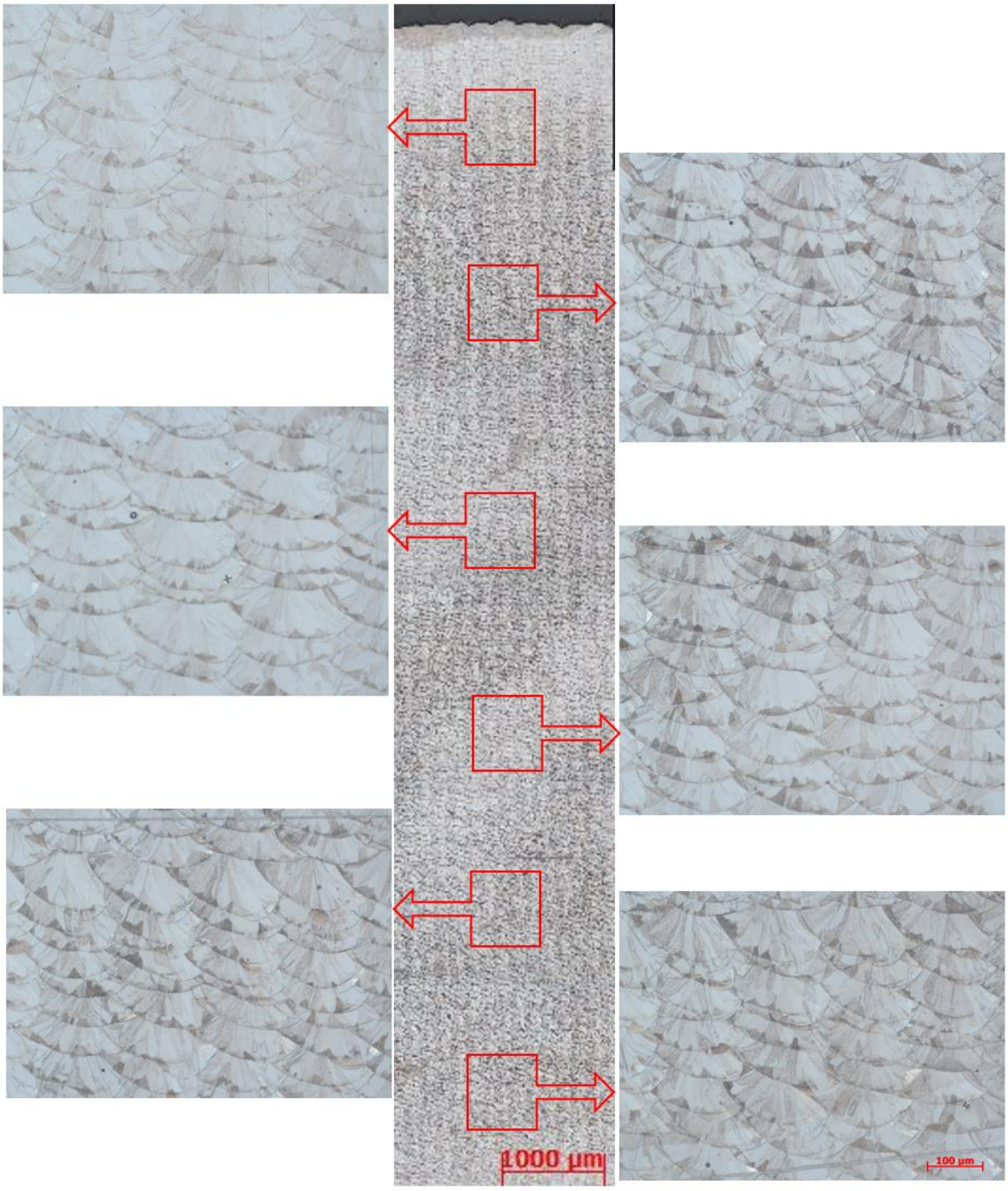

Figure 2.4 Melt pool and grain image of graded hatch spacing process parameter.

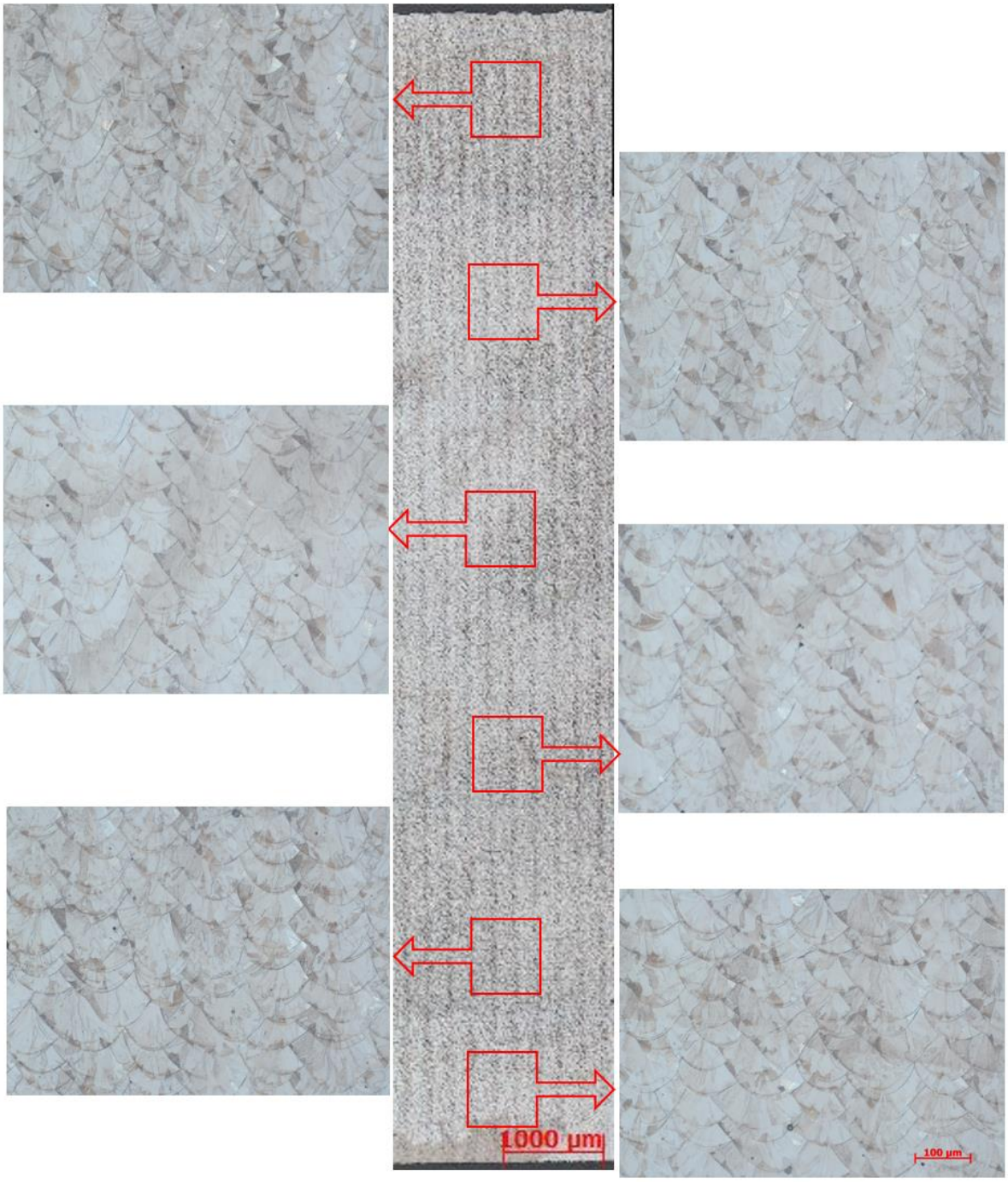

Figure 2.5 Melt pool and grain image of graded scanning speed process parameter.

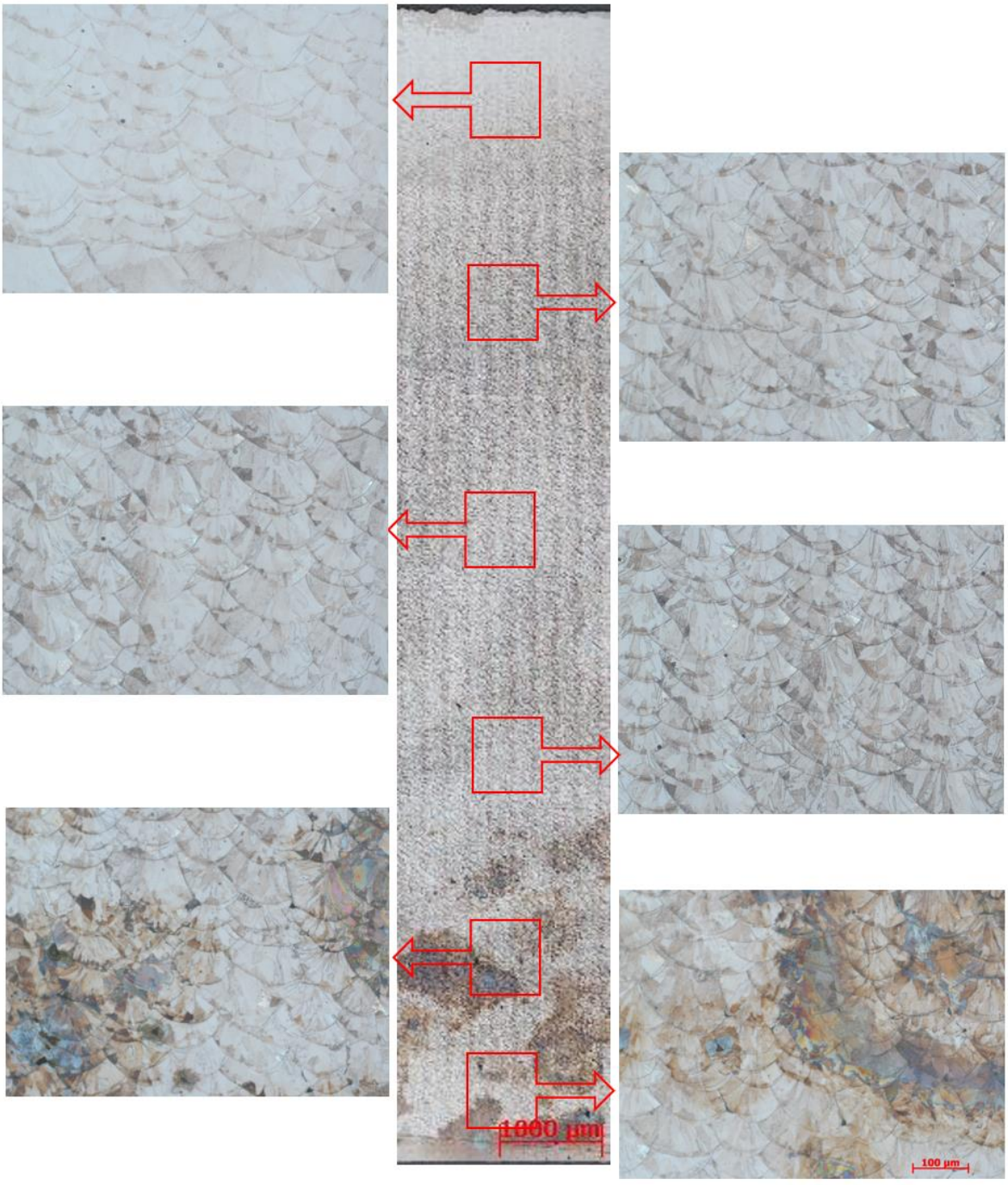

Figure 2.6 Melt pool and grain images of graded scan speed and laser power process parameters.

Further images were taken using the Zeiss LEO 1550 Scanning electron Microscope (SEM). This machine is a high-performance Schottky field-emission SEM used for high-resolution imaging of surfaces and qualitative analysis [24]. This instrument is used for obtaining material information and uses a focused, high-energy electron beam. The beam is deflected and moves in a pattern scanning the surface of the object [25].

The samples were each placed in epoxy, which was not conductive to allow for the images to be taken using this microscope; thus, a conductive tape needed to be employed placed on the edge of the sample's surface and connect the specimen to the sample holder. Once the sample was prepared for imaging, the images were taken under the secondary electron detector to depict equiaxial cell size throughout the samples. The samples were imaged under an electron high tension (EHT) voltage of 5kV.

Each SEM image was taken was at each level where a parameter had been changed in the sample vertically, along with images along the horizontal axes to provide an average at each parameter (Figure 2.7). Approximately 25 images were taken at each of the MGM samples' surface and used for further analysis. These images were then imported into ImageJ software to get an approximate average area of the cell size. Figure 2.8 and Figure 2.9 show some of the SEM images taken at different regions in the samples.

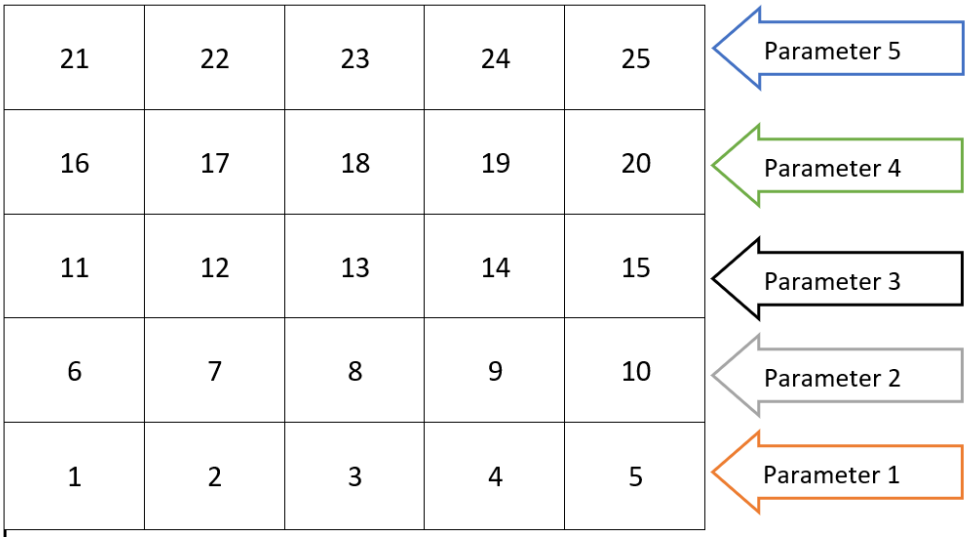

Figure 2.7 SEM image schematic to show how many images were taken of each sample for characterization. Five images were taken at each parameter in the sample for the 10 by 10-millimeter specimen.

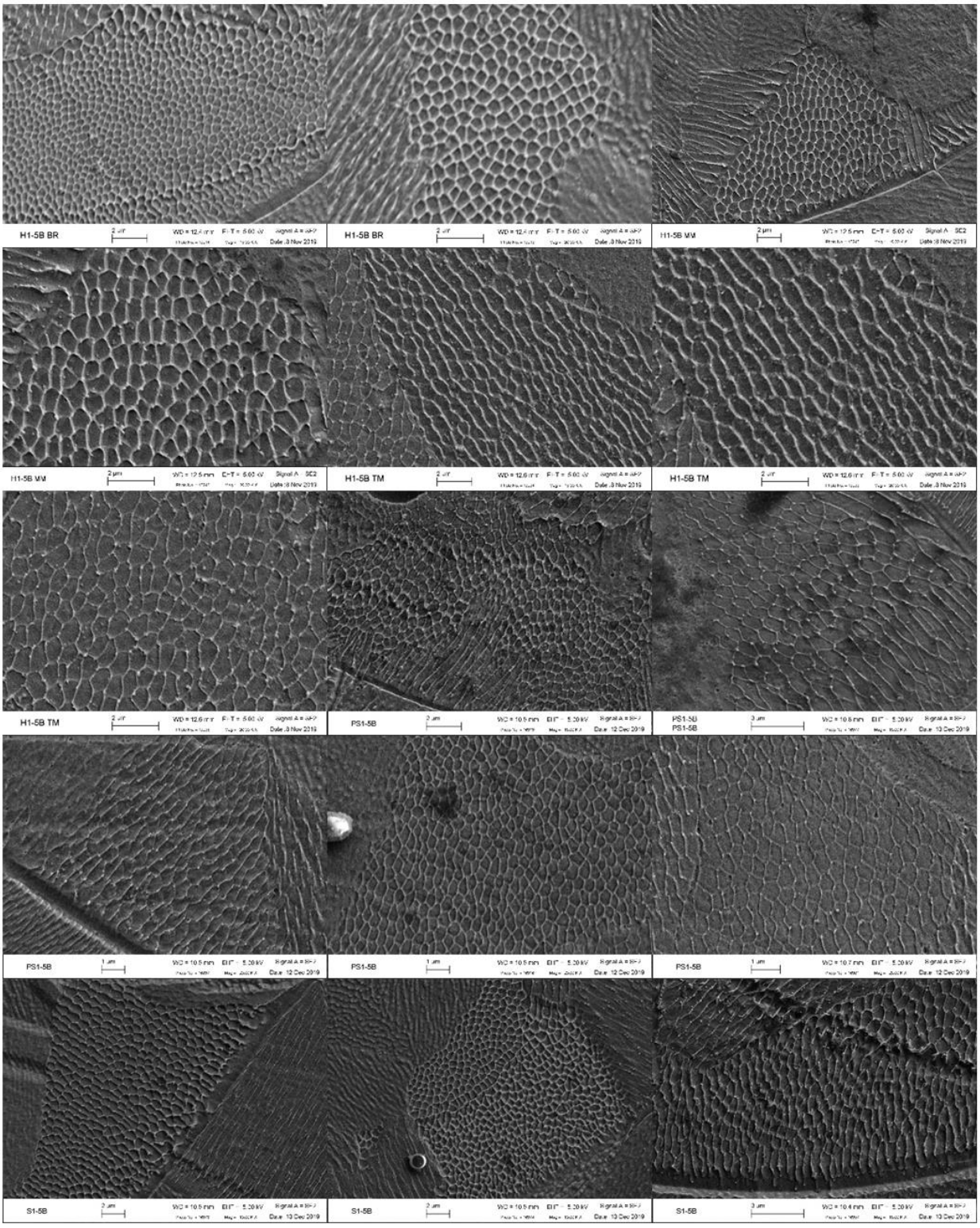

Figure 2.8 SEM images of equiaxial cells at various locations for the graded process parameters.

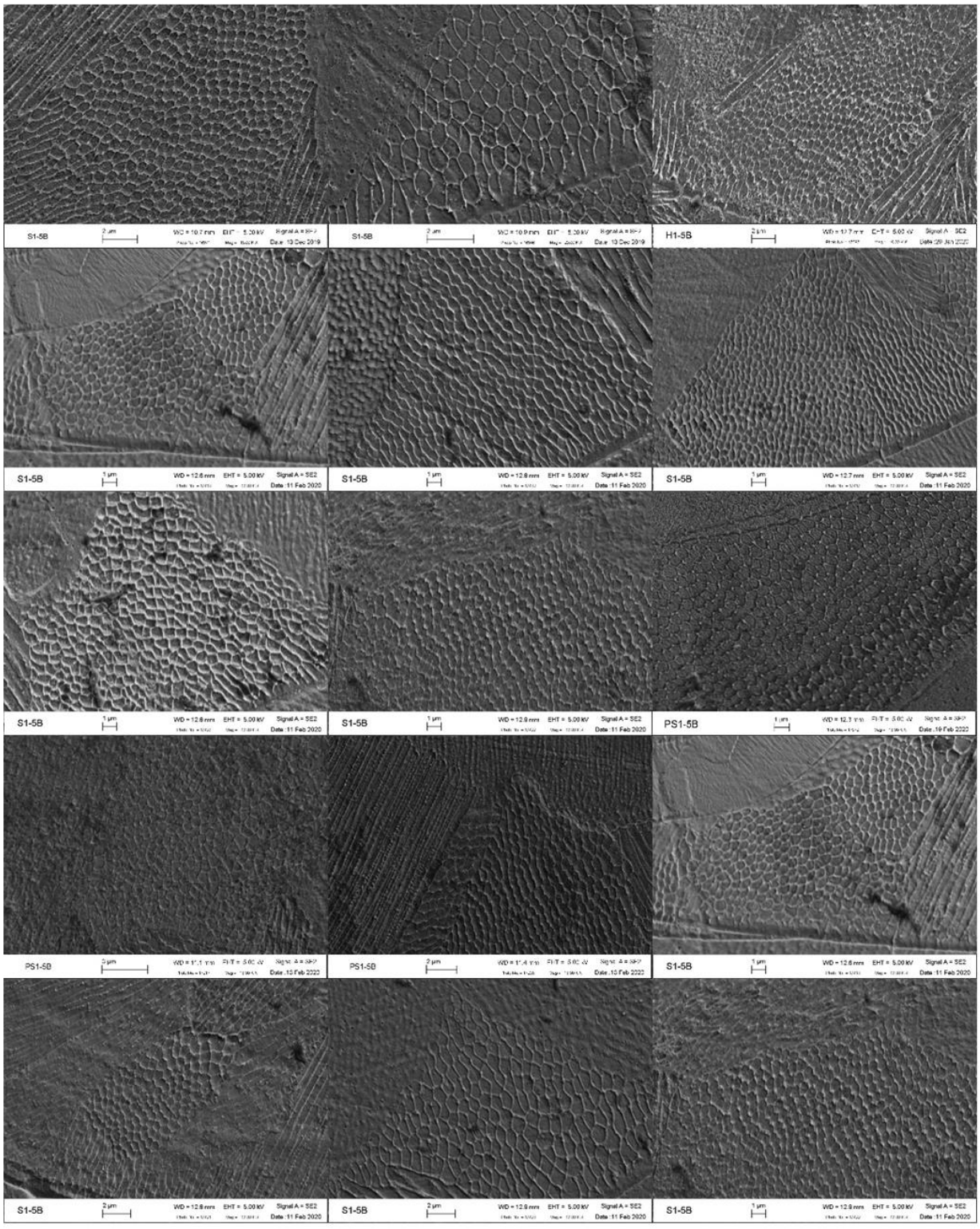

Figure 2.9 SEM images of equiaxial cells at various locations for the graded process parameters.

2.2.3 Image Processing Method

Image processing was implemented using the optical and SEM images taken to determine cell and melt pool characteristics. The images were imported into ImageJ [26] for analysis. The scale was incorporated into the measurements, and the image was cropped to include only a section of equiaxial cells. The image was then converted to a black and white binary image for the software to analyze (Figure 2.10). Depending on the cellular growth direction, cells can be either equated or elongated. Cell formation is attributed to the direction of the temperature gradient [27] during the build process. ImageJ software allows the user to analyze "particles," or in this case cells and melt pools, and outputs each cell's area and analyzes this data to provide average area and distribution characteristics of the chosen area.

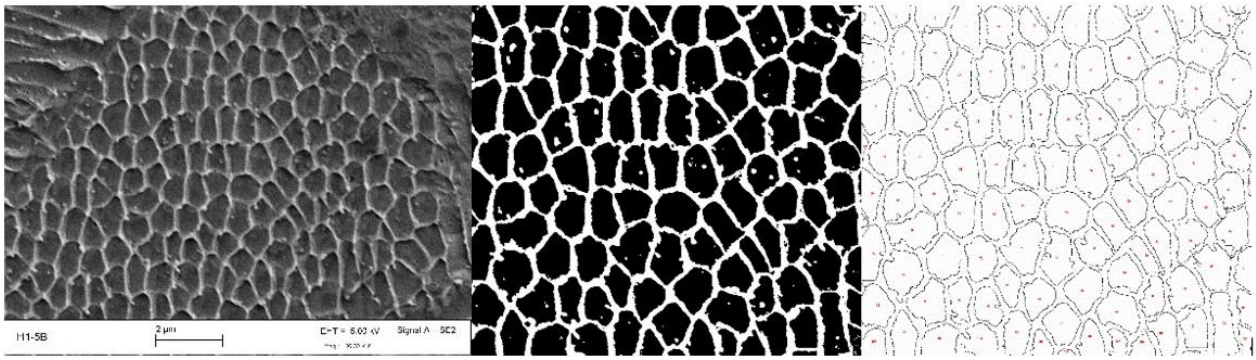

Figure 2.10 Image J Analysis process for equiaxial cells.

The software takes the binary image and uses the cells in black while excluding the defects in the binary images smaller than a given size to count the number of cells and each cell's size and other variables if chosen. For this investigation, only the area of the cells was used for analysis.

Along with the cells, ImageJ was used to characterize the grain area, melt pool width, area, depth, track-track boundary, and layer- layer boundary (Figure 2.11). The layer-layer-boundary refers to the lower portion of the melt pool where the melt pools are layered above

one another. The track-track boundary is a boundary within the melt pool, where the melt pool overlaps with the melt pools on the top or bottom and to the left or right. The melt pool width and depth were calculated by tracing various melt pools in their entirety (Figure 2.12) in the optical images and then converting them to binary to be analyzed similarly to the equiaxial cells. The same process was used for the grain area. The melt pool boundary characteristics were traced, and the length of each trace was outputted at various locations.

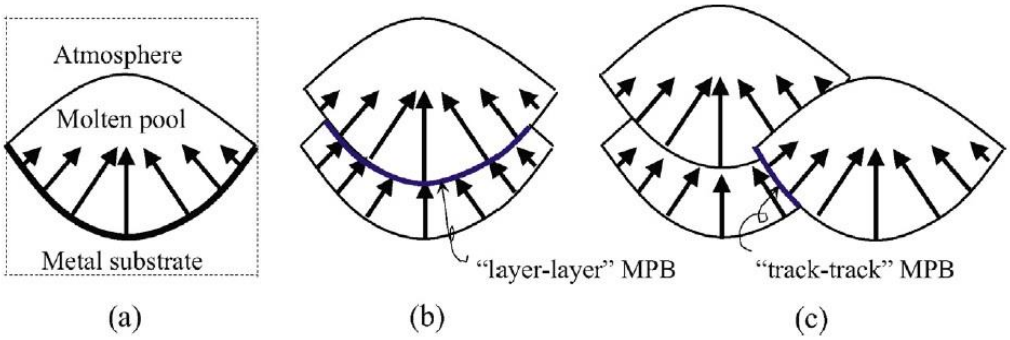

Figure 2.11 Schematic of (a) Melt pool boundary, (b) "layer-layer' boundary, and (c) "track-track" boundary within the stacking of the melt pools. [28]

With the output from each image analyzed, the average of each of these characteristics was compared for each printing parameters throughout the SLM fabricated specimens. The output from the ImageJ analysis was used to provide further quantitative investigation.

Figure 2.12 Overlay image of melt pool tracing on the optical image to determine average melt pool characteristics.

Analysis in MATLAB was conducted on normal distribution and trend of cell area, grain size, and melt pool area. MATLAB is a programming language that allows for numeric computation. The remaining melt pool descriptors, including depth, width, layer- layer boundary, and track- track boundary, were only analyzed using the outputs from ImageJ. A table with the values for their average sizes was created.

2.3 Results and Discussion

2.3.1 Visual Analysis of Optical and SEM Microscopy

Initial analysis began with observing the optical and SEM images of these MGM samples. Optically, the melt pool and grains were reviewed to determine if any key characteristics can be seen visually. From a visual analysis of the optical images, each of the varied process parameters' melt pool boundaries can be seen clearly at each step. There are discolorations within the melt pools and between the boundaries, which show the material's grains.

Within the MGM with the changing hatch spacing, the melt pools' effect is evident as the parameters change. Figure 2.4 shows that the hatch spacing is increased, showing that the melt pool width increases and the depth decreases. While all parameters remain the same, including laser power and scanning speed, the spacing between each pass of the laser increases. So, as the molten materials solidify and the spacing increases, the size of the melt pool changes. The increase in hatch spacing size resulted in the reduction of the cooling rate, which affects the microstructure. Other variables that appear to be affected as the hatch spacing increased is the overlap rate, which decreases, along with the temperature gradient. The epitaxial grain growth

in hatch MGM is more prominent as the hatch spacing is smaller because of the higher temperature gradient.

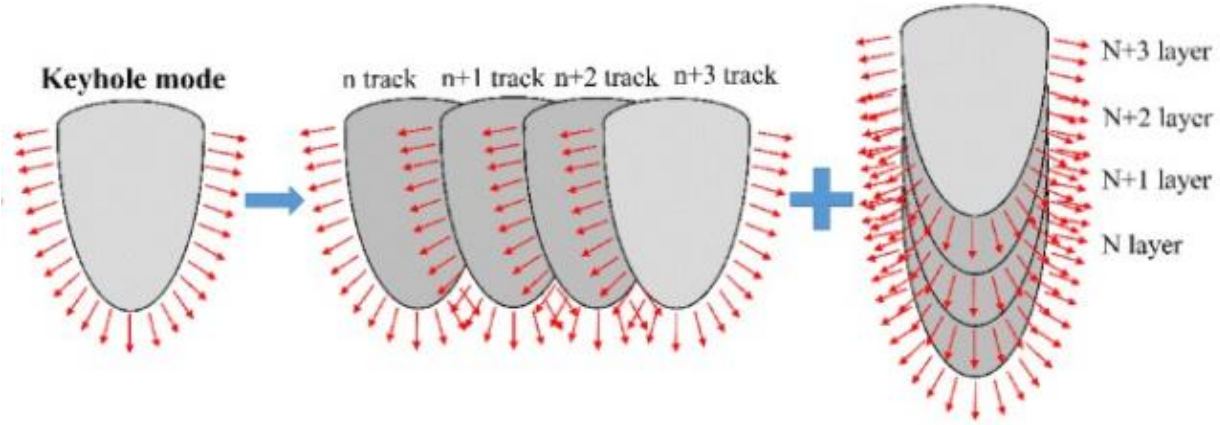

Figure 2.13 Keyhole formation schematic with heat gradient [29].

With a change in scanning speed, to build these MGMs, some specific characteristics are present in the melt pools and grains. The grains become more significant in the specimens as the speed decreases (Figure 2.5) due to the higher temperature. In the graded speed specimen, melt pools were deeper with a narrowing impression in the liquefied material; this is referred to as a keyhole (Figure 2.13). Keyholes occur by introducing a high energy source, considerable penetration depth, and a small heat zone [13]. Some researchers state that the keyhole melt pool affects the part's quality due to the formation's instability [30, 31]. These optical images visually gave great insight into what is happening throughout the entire specimen's structure, where the SEM images provided information at the cellular level. In Figure 2.6, over-processing occurs when the power and speed parameters were 200W and 0.80 m/s due to higher porosity, faster speed, and higher power. The parameters change throughout the etchant's specimen material changes with the parameters. As the speed and power are larger, the grain formation is smaller due to the reduced cooling time it experiences during the build [32]. The melt pools in

the laser power and scanning speed MGM do not show a clear trend visually. It appears that epitaxial grain growth shows some irregularities as some grains are smaller in size and do not show a clean epitaxial growth through the melt pool.

SEM images provided the basis for qualitative analysis of the microstructure on the sample. One of the critical characteristics to note is that in particular images, the unconsolidated powder can be seen in Figure 2.14. Unconsolidated powder refers to powder particles not being fully melted in the printing process. The presence of these powder particles can lead to cellular formation disparities, which can ultimately lead to mechanical properties. It is more likely for a dislocation to occur at these locations since there is no uniformity within the microstructure.

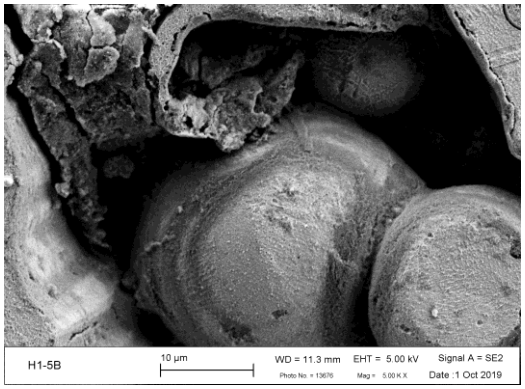

Figure 2.14 SEM image of unconsolidated powder in Hatch spacing.

The smaller hatch spacing cells appear to be more distinct and begin to become ambiguous as the hatch spacing increases. This trend was less apparent in the remaining MGM specimens. Within the melt pools, the SEM revealed the cellular structure included the equiaxial and elongated cells. For this research, the equiaxial cells were quantitatively analyzed due to uniformity in shape. The cell area average and standard deviation of each level per Figure 2.7, with a varying parameter, was then used to provide graphical results. Each

parameter in the hatch spacing, scanning speed, and laser power, and scanning speed, revealed specific characteristics relating to the process parameters effect on the microstructure.

2.3.2 Image Processing of Microstructure for MGM Specimens

Through the ImageJ program, the optical and SEM images were used to develop cellular and melt pool characteristics. The cellular area was average at various locations along each of the gradient parameters in each build and the melt pool boundary characteristics. The mean average cell area and standard deviation of the sample size of cells chosen from each SEM image were analyzed.

In the hatch spacing MGMs, the cells' normal distribution at each of the five spacings chosen was plotted from ImageJ. As the hatch spacing, shown in Figure 2.15(a), increases the standard deviation and mean increase. At 75-micron hatch spacing, the average cell area was approximately 0.20 μm^2, and there was a small distribution of this area. This distribution suggests that the cells' area is more consistent and smaller compared to a higher hatch spacing. At the two highest hatch spacings characterized, there is less deviation between the mean cell area. The distribution of the area is also more consistent with each other than the three smaller hatch spacings. The mean and standard deviation for each printing parameters' cell area shows a trend. As a result, of gradually changing the hatch spacing, it can be concluded that the cells' area will increase as well and may begin to be less distributed as the spacing increase and if complete melting and solidification occurs. This assessment does not include porosity or unconsolidated powder, which is likely to increase as the hatch spacing increases.

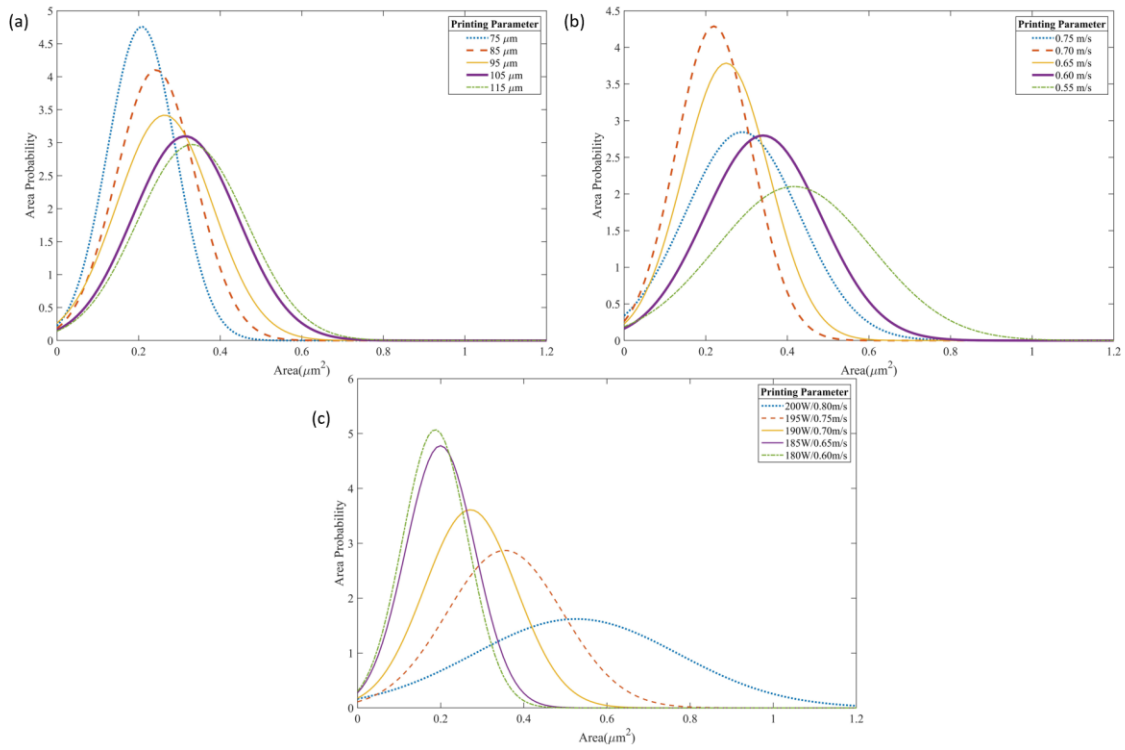

Figure 2.15 Normal distribution plots of (a) Hatch spacing, (b) scanning speed, and (c) laser power and scanning speed for each parameter used in the graded specimens.

The scanning speed distribution is not as uniform and shows no definite trend (Figure 2.15b); as the speed decreases from 0.70 m/s to 0.55 m/s, the mean and standard deviation increase. However, for the speed of 0.75 m/s, this outlier shows a mean between 0.65 m/s and 0.60 m/s, and the standard deviation is between 0.60 m/s and 0.55 m/s. This can result from the interaction between the constant power of 200W and the current scanning speed and can also be attributed to the higher cell area in the images chosen for analysis. Compared with the varying laser power and scanning speed at power 190W and speed of 0.70 m/s, the mean cell area was closer to 0.30 µm², which is consistent with the speed of 0.75 m/s. Then as the speeds decrease with the constant power of 200W, the average cell area increases along with the distribution. As the speed and laser power decreases, the mean cell area decreases, and the distribution becomes less skewed. A higher power results in instability amongst the cells' size

due to the variations in the temperature while increasing speed. Overall, when comparing the cell area between each parameter, the mean cell area's distribution is closer in scanning speed and hatch spacing than in the laser power and speed parameters.

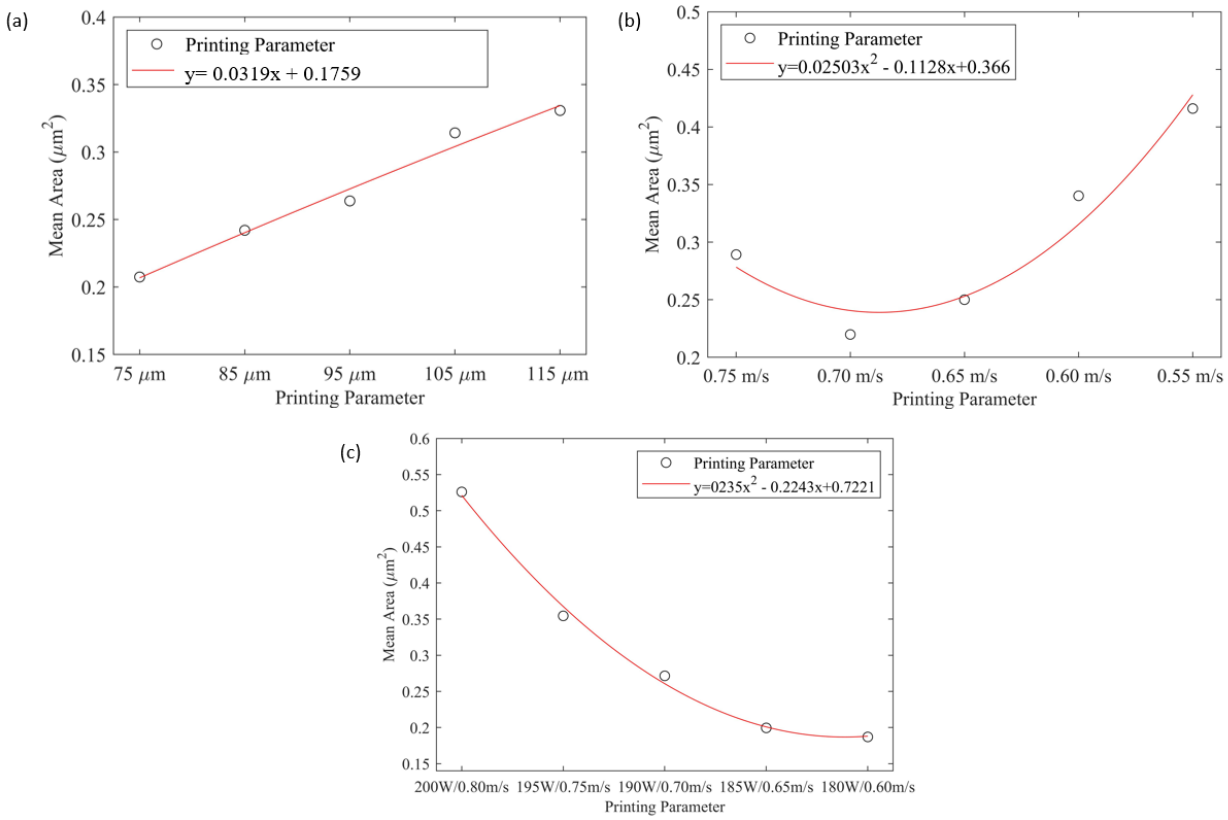

Figure 2.16 Trendline plots of each of the specimen's mean area at the designated parameters of (a) hatch spacing, (b) scanning speed, and (c) laser power and scanning speed.

From these standard distribution plots, a general trend of the equiaxial cell area can be determined. Furthermore, this data was used again to show each sample's general trendline (Figure 2.16). These plots provide an equation for the polynomial curve trendline. The cell area for hatch spacing is increasing as the spacing increases linearly. As the power and speed decreases, the cell area also decreases. There is less trend certainty in the speed sample due to the high area at a speed of 0.75 m/s compared to the other speeds.

Similarly, with the cell area, the melt pool area was analyzed using optical images. Various melt pools were selected at each area where a parameter changed and analyzed with the same image processing method. Clear trends in melt pool formation can be seen within these parameter sets. As the hatch spacing increases, the cell area and melt pool size increases (Figure 2.17a). The actual values of the cell area, when compared to the trendline, show the little deviation between the parameters. However, for the scanning speed, even though the melt pool area increases, there is a higher deviation in the trend. It appears that the melt pool area for the scanning speed of 0.70 m/s is significantly lower than the trend, but the cell area does not appear to have the same trend as the melt pools.

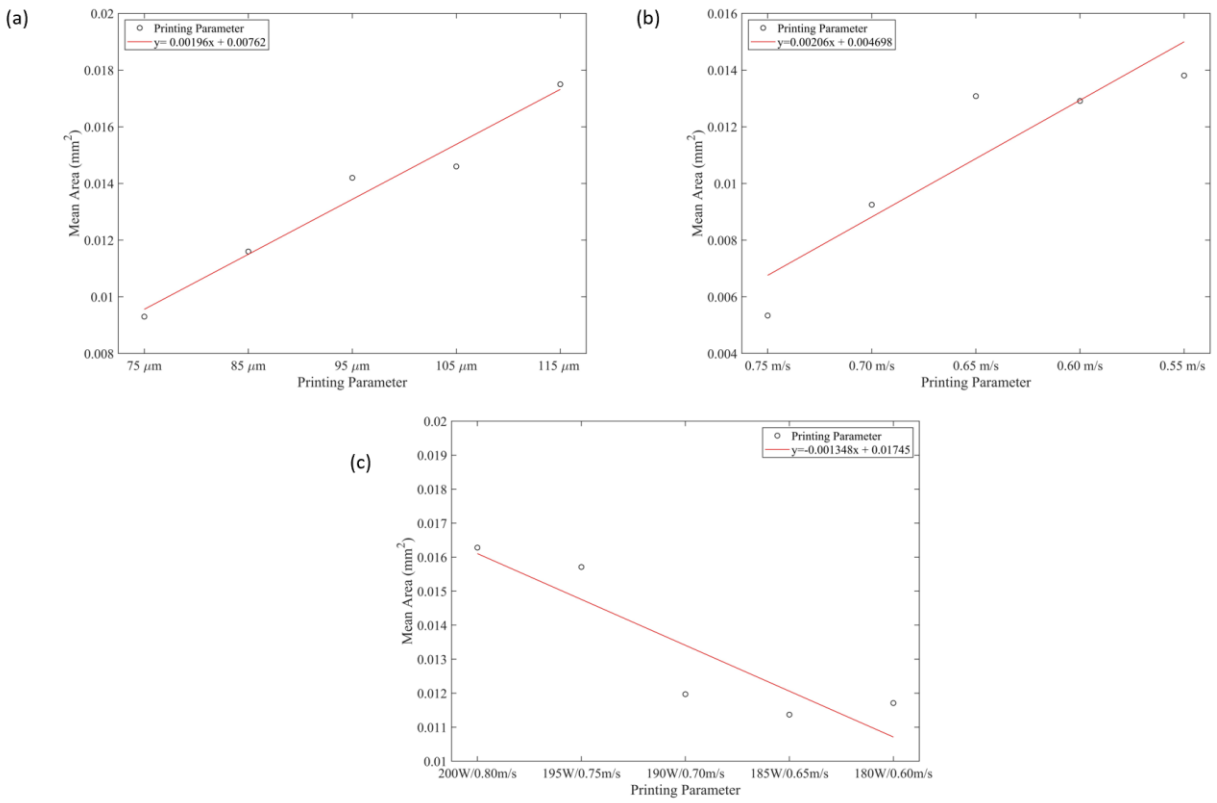

Figure 2.17 Trendline of the melt pool area in (a) hatch spacing, (b) scanning speed, (c) laser power and scanning speed.

Along with the melt pool and cell area analysis, the averages of the track-track and layer-layer boundaries, grain area, and melt pool depth and width were characterized. The image processing results of these additional characteristics are shown in (Appendix A). In the future, the results from this table can be used to create a model that can track which parameters to use to receive one of the results for the melt pool characteristics.

Chapter 3

3. Experimental Analysis of Materials with Graded Microstructure

3.1 SLM Fabrication and Parameter Selection

Analysis of the three sets of process parameters, hatch spacing, scanning speed, laser power, and scanning speed, provided a basis of the cellular and melt pool formation during each of these parameters. With the results of that analysis, one set of process parameters were chosen to be tested mechanically. Mechanical testing provides material information relating to the strength, failure, and fatigue life. Within the MGM sample, where the laser power and scanning speed were changed, the cellular formation showed a decrease in the area faster, as the power and speed decreased. The interaction between these parameters and the effect on the material still left some uncertainty and resulted in selecting these parameters for the mechanical performance analysis.

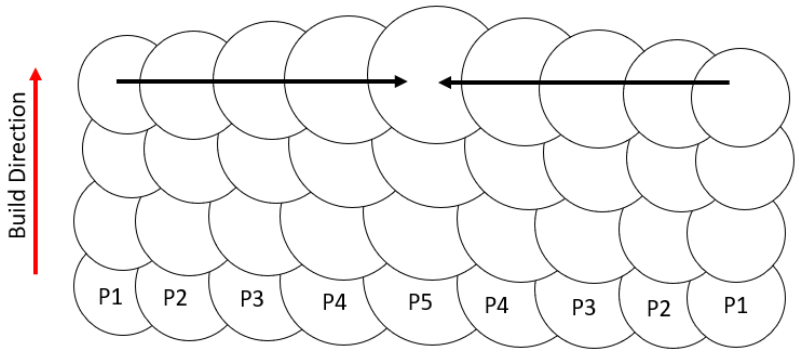

Figure 3.1 Melt pool schematic of the graded specimen, with build direction and parameter change direction, with smaller melt pools along the edges.

To create the MGM, the desired microstructure formation was determined. The goal was to design, and SLM fabricated MGM with smaller microstructural characteristics on the edges of the specimen to the left and right and increase the melt pools' size towards the center. When

cells and melt pools are small, it has a higher mechanical performance. Current research examines the effect on the mechanical properties as the sample is tension tested where the parameters change in the build direction [33-35]. These works conclude that the sample is more likely to fail at the locations where the parameters change attributed to larger dislocations and crack propagation.

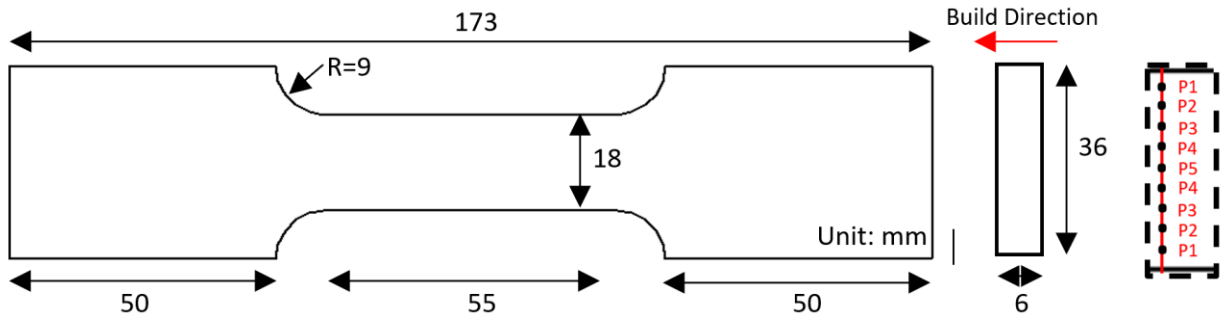

Figure 3.2 Schematic of SLM fabricated dog bone specimen with printing parameter designation.

Due to these articles' results, the samples were built where the parameters changed throughout the cross-section of the specimen from left to right (Figure 3.1). Parameters are the same on the outer edges and changes as it goes towards the center. When the sample is mechanically tested, the initial reaction will occur at laser power and speed with smaller cells and melt pools. The dog bone specimen was built on the Renishaw AM250, changing the laser power from 180W to 200W and the scanning speed from 0.60 m/s to 0.80 m/s. The sample was printed lying flat, where the build direction was parallel through the thickness (Figure 3.2). ASTM E8/E8M – 13A was used as a basis to determine tensile specimen dimensions and was adapted to fit experimental setup. Along with the graded sample built, additional dog bones were printed with consistent laser power and scanning speed, and the parameter sets P1, P3,

and P5, for comparison. The parameters are listed in Table 3-1 for the graded specimen, where P1, P3, and P5 are the parameters for the constant specimens.

Table 3-1 Printing parameter for graded dog bone specimen according to the schematic in Figure 3.2.

Parameter	Power (W)	Speed (m/s)
P1	180	0.60
P2	185	0.65
P3	190	0.70
P4	195	0.75
P5	200	0.80

3.2 Mechanical Testing Methods

3.2.1 Tension Testing

Mechanical testing is performed for the mechanical response on the MGM, and consistent samples to compare properties. Two of each type of specimen, MGM, and constant parameter samples, were tensile tested. Only two samples were tested due to limited number of samples. Uniaxial tensile testing was conducted using both hydraulic and screw driven Instron machines. Initially, the hydraulic machine was tested to provide mechanical performance; then, these samples were used for fractography. Samples were uniaxially tensile tested a second time on the screw-driven machine for additional variables and because the screw-driven machine is where the low cycle fatigue testing was conducted.

The testing criterion under both machines was similar to reduce any deviations. The graded specimen and constant specimens were tested using each machine in displacement control. Samples were placed in the wedge holder, and a strain extensometer was attached to the

gauge section. The extensometer used on the hydraulic machine had a gauge length of 1 inch, and the one used on the screw-driven machine was a 2 in extensometer. Each specimen was pulled to failure at a displacement rate of 2 mm/min. The hydraulic tension test strain was measured through the extensometer up to 50% strain, and the reaming strain to failure was measured based on displacement. The machine outputs raw data for the stress in MPa and strain in percentage values during the test, and these were analyzed to determine mechanical performance.

3.2.2 Fatigue Testing via Cyclic Loading

The low cyclic fatigue (LCF) life was tested using the screw-driven tensile machine with a triangular wave formation (Figure 3.3). LCF is where the plastic strain occurs and observes areas with larger cycles and plastic deformation. LCF analysis is reviewed in conditions of a short life. One MGM specimen and one of each of the constant parameter specimens were fatigue tested, due to limited number of samples. Each of the tests used the maximum yield stress results from the tensile response on the screw-driven machine to determine the stress range. An R-ratio of 0.1 was used for the stress-controlled system, with a displacement rate of 0.1mm/sec. The R-ratio, or stress ratio, is the minimum stress ratio to the maximum stress applied during the cycle. The 2 in extensometer measured strain for the loading, and the test was under full tension and did not go into loading compression using a 2 in strain extensometer.

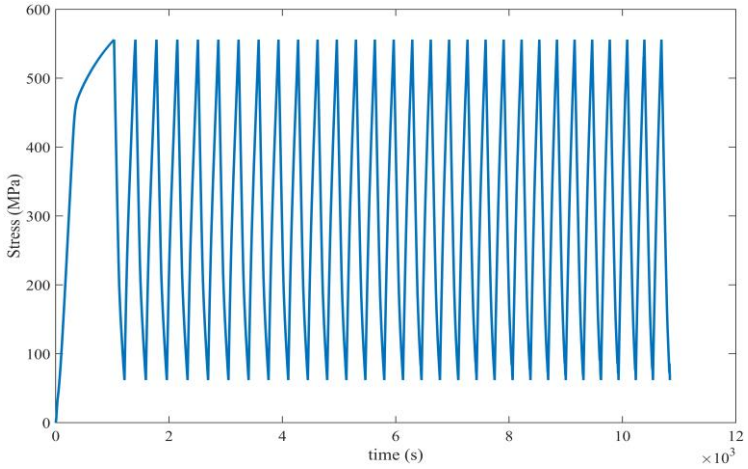

Figure 3.3 Triangular waveform for cyclic loading under stress-control.

The cycle count was 30 for each specimen, and their Stress-Strain curves were plotted, the first five cycles along with the tenth, twentieth, and thirtieth cycles. The yield stress was calculated from each of these tests along with the ratcheting strain. Ratcheting strain describes the progression of the hysteresis loops quantitatively, and plastic accumulation development and the ratcheting strain rate change in ratcheting strain as the cycle count increases [36]. Ratcheting strain can be quantitatively written in the equation,

$$\varepsilon_r = \frac{1}{2}(\varepsilon_{max} + \varepsilon_{min}) \quad (1)$$

Where ε_{max} is the maximum strain during the cycle and ε_{min} is the minimum strain. The hysteresis loop and ratcheting strain depend on the loading stress.

3.3 Tensile Analysis and Results

The samples that were tension tested were used for analysis to determine the mechanical properties of both the MGM and constant parameter specimens. These tests were performed on as-machined surfaces. The specimens' original gauge length was 55 millimeters, and the uniaxial tension tests failed at approximately 50-57% strain, which is a

displacement of 27.5-31.75 millimeters. The original gauge length was compared with the tested tensile samples visually (Figure 3.4) and depicts that the original gauge length is significantly smaller than the tension tested specimens.

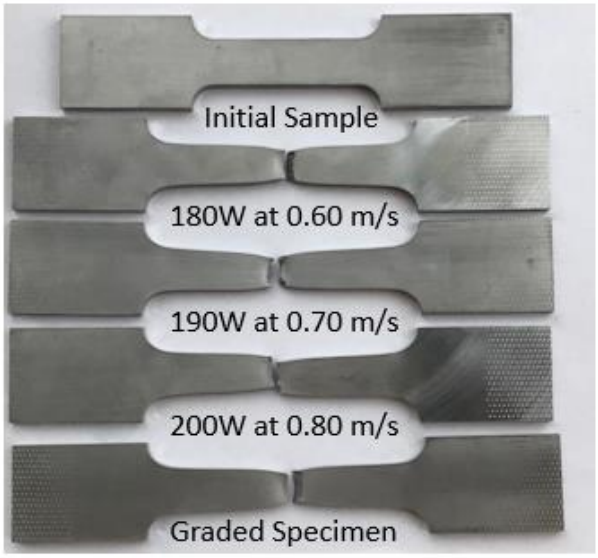

Figure 3.4 Uniaxial tension tested MGM and constant parameter specimens gauge length, compared to the original specimen.

Visually, during the test and in Figure 3.4, necking occurs when the cross-section area begins to reduce after ultimate tensile strength is reached [37]. The gauge section's width has decreased significantly, which is where the reduction in the area can be seen. The tests' raw data were analyzed to plot the Stress-Strain curves (Figure 3.5).

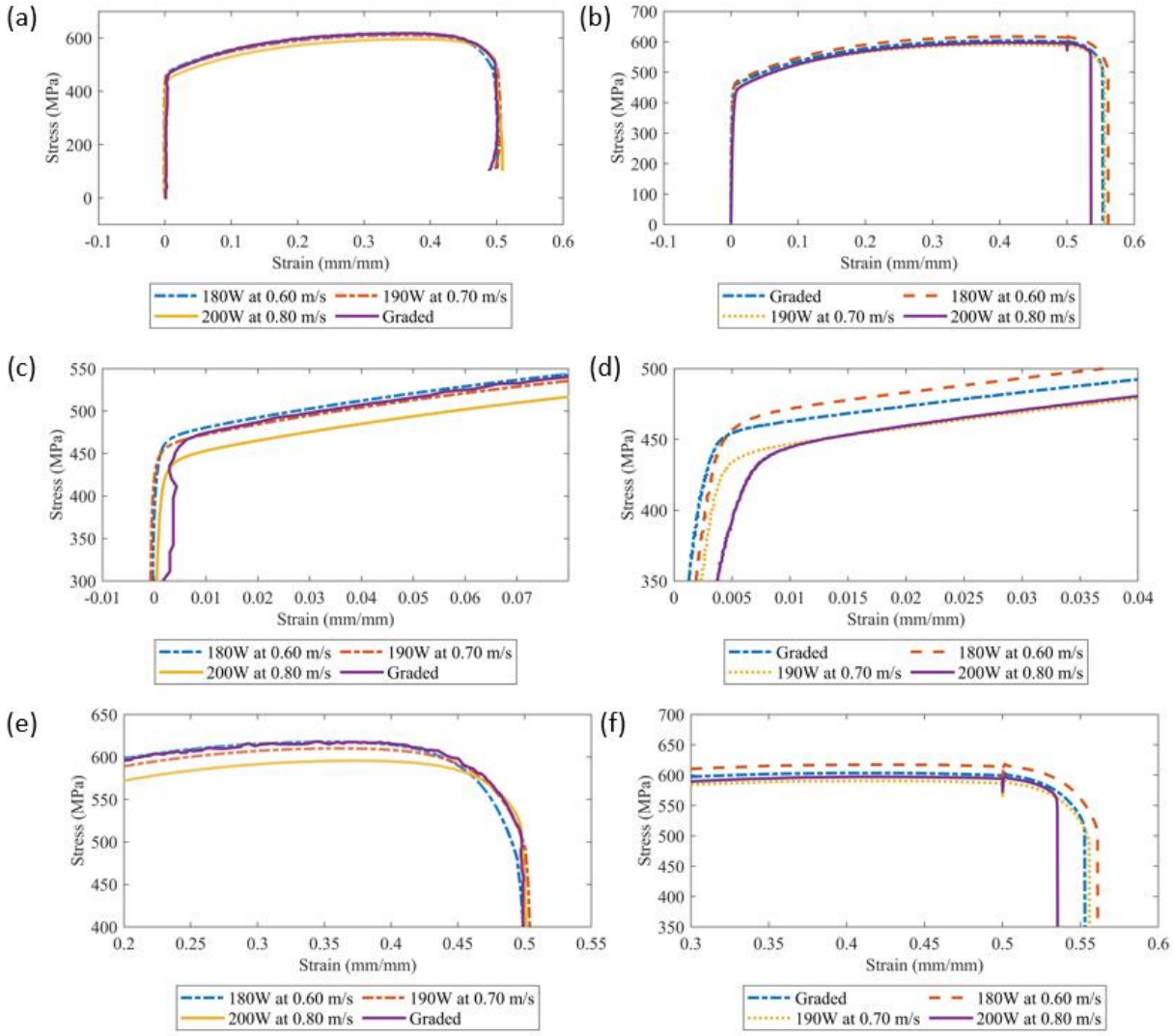

Figure 3.5 Tensile response at each machine, where (a) and (b) are the results from the entire test of each specimen, (c) and (d) is the zoomed-in location where the yield occurred, and (e) and (f) is the area where the UTS and break occurs. The figures' left column are the results from the screw-driven machine, and the right column is from the hydraulic tension machine.

The plots show that the 180W at 0.60 m/s samples performed the best in terms of yield strength and Ultimate Tensile Strength (UTS), where the graded specimen was near these results as well, and the remaining specimens fell below on performance. The largest difference between the machines in terms of results is the elongation at break. Samples testing using the screw-driven machine failed at a faster strain than the other specimens. This is due to the

change in the strain extensometer and the extensometer's removal during the hydraulic testing. The curve where the break begins has a more gradual change in the screw-driven tests, whereas the hydraulic tests did not. From these results, it can be concluded that the graded specimen's mechanical properties performed closer to the lowest speed and power, but not as well as that parameter set.

The raw data was used to plot the Stress-strain curves, and then the elastic region of each plot was analyzed to get the linear response. The 0.2% yield offset was calculated and reported from these results, along with UTS and elongation at break (*Table 3-2*).

Table 3-2 (Table A) Tensile testing machine characteristics and analyzed UTS results, elongation at break, and YS. (Table B) Percent difference in UTS, elongation, and yield strength compared to MGM specimen.

Table A	**Machine**	**Extensometer (Gauge Length)**	**Ultimate Tensile Strength (MPa)**	**Elongation at Break (%)**	**Yield Strength (MPa)**
MGM Sample 1	Hydraulic	1 in	603.7	55.3	439.45
1A 180W, 0.60m/s	Hydraulic	1 in	618.3	56.1	439.21
3A 190W, 0.70 m/s	Hydraulic	1 in	590.8	55.6	430.35
5A 200W, 0.08 m/s	Hydraulic	1 in	597.4	53.5	399.95
MGM Sample 2	Screw-Driven	2 in	618.2	50.2	466.57
1B 180W, 0.60m/s	Screw-Driven	2 in	617.8	50.1	462.43
3B 190W, 0.70 m/s	Screw- Driven	2 in	610.2	50.0	452.44
5B 200W, 0.08 m/s	Screw- Driven	2 in	595.6	49.9	432.85

Table B	**Machine**	**Ultimate Tensile Strength (MPa)**	**Elongation at Break (%)**	**Yield Strength (MPa)**
MGM Sample 1	Hydraulic	0	0	0
1A 180W, 0.60m/s	Hydraulic	2.42	1.45	-0.05
3A 190W, 0.70	Hydraulic	-2.14	0.54	-2.07

m/s				
5A 200W, 0.08 m/s	Hydraulic	-1.04	-3.25	-8.99
MGM Sample 2	Screw-Driven	0	0	0
1B 180W, 0.60m/s	Screw-Driven	-0.06	-0.20	-0.89
3B 190W, 0.70 m/s	Screw- Driven	-1.29	-0.40	-3.03
5B 200W, 0.08 m/s	Screw- Driven	-3.66	-0.60	-7.23

All samples tested with the hydraulic machine have an elongation percentage between 53.5% and 56.1%, whereas the ones tested using the screw-driven machine had a range between 49.9% and 50.2% elongation. The difference in elongation can be attributed to the strain gauge being removed during the hydraulic tensile tests. The graded sample at the sample 180W at 0.60 m/s performed closer than the other two parameters, which is most likely due to the grade specimen's edges having the 180W at 0.60 m/s parameter on the edges. The UTS decreased as Power and speed decreased, and similarly to yield stress and elongation, the graded specimen performed below 180W at 06 m/s and above 190W. The percent difference for each of the mechanical properties of each specimen was calculated in comparison to the MGM specimen. Within the screw driven machine, it shows that the UTS, yield strength, and elongation at break all have a negative difference which suggests that the MGM sample is the strongest in terms of these properties.

3.4 Fracture Analysis

In conjunction with the tensile analysis, the tensile specimens' surface was imaged using an LEO FESEM. Fracture microscopy gives qualitative insight into how a specimen failed a

comparison and the surface features of the fracture. The full fracture surface sections were imaged and stitched together to depict the entire fracture surface (Figure 3.6).

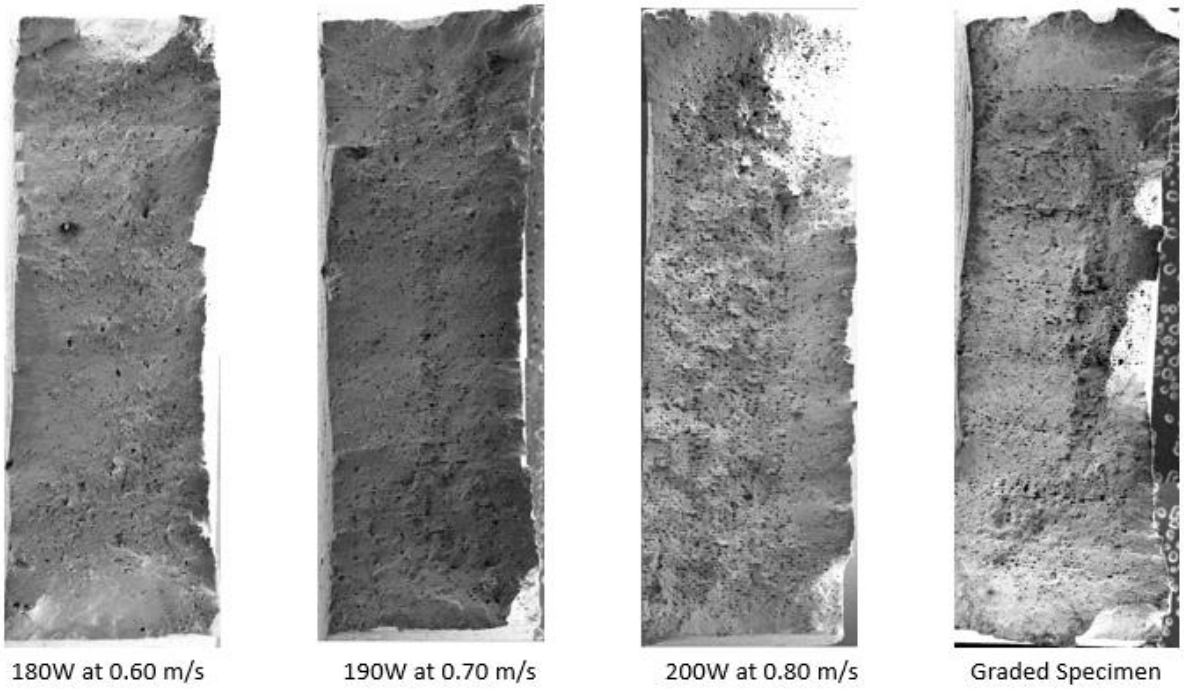

Figure 3.6 Complete fracture surface of each sample.

Fracture is initiated when small voids begin to form within the microstructure. These voids begin to form cracks and these cracks propagate, which leads to fracture. From these micrographs, porosity is seen throughout each of the specimens. The highest power and speed have the largest porosity, and this same parameter within the MGM can be seen at the center of the image. In both the 190W and 200W micrographs, it appears that fracture occurred within the center of the sample perpendicular to the build direction. The graded specimen failed at the center of the specimen towards the micrograph's right and tearing occurred. The fracture propagated from the location where it is weaker; however, from the tensile test, the sample's strength is like the slowest laser power and scanning speed tested.

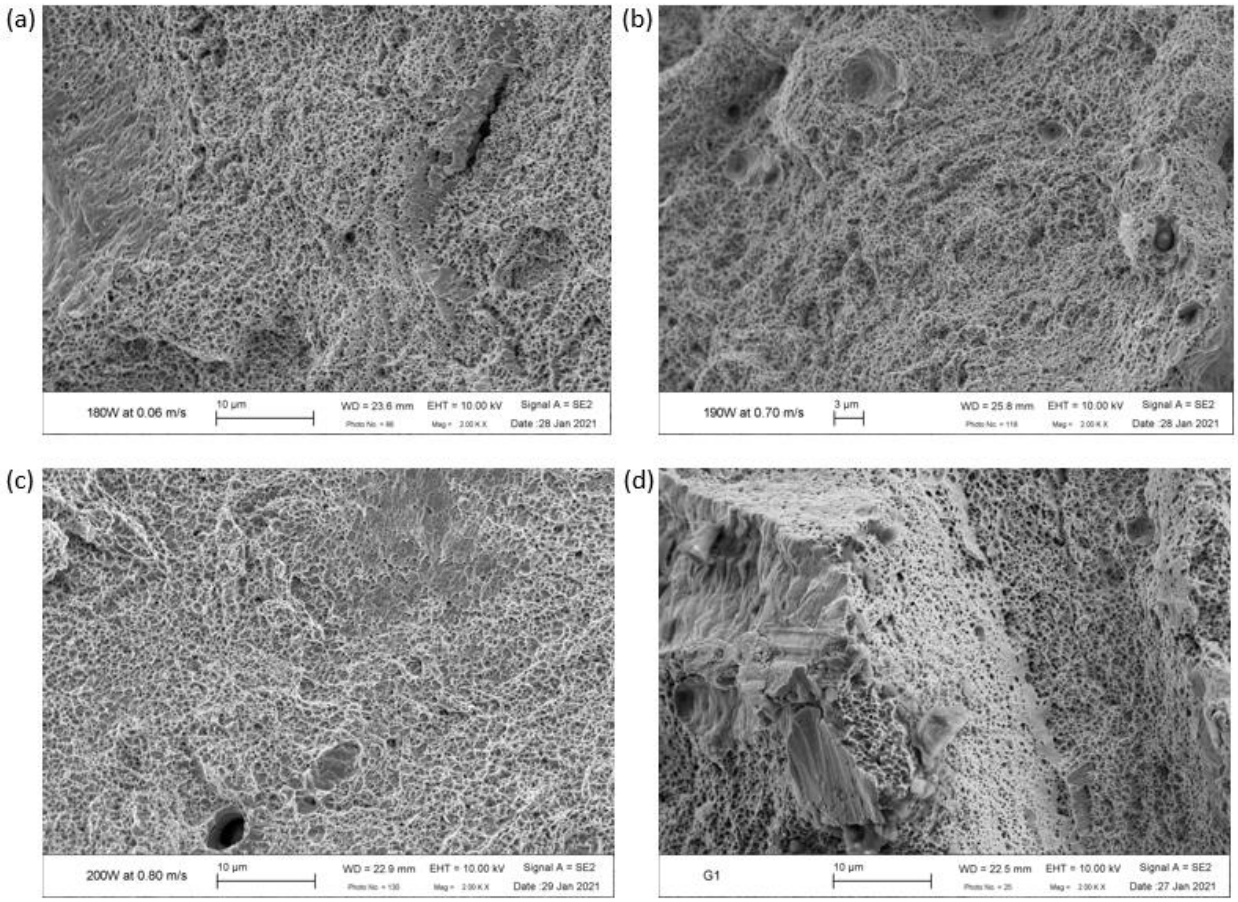

Figure 3.7 fracture microscopy and different locations (a)180W at 0.60 m/s, (b) 190W at 0.70 m/s, (c) 200W at 0.80 m/s, and (d) MGM specimen

The zoomed-in micrographs at a location on each fracture surface (*Figure 3.7*) provide characteristics of the type of fracture that occurred. There is significant porosity in these materials, which can lead to weaker mechanical properties. There is significant dimpling that can be seen on each of the surface micrographs, which implies ductile fracture. Ductility refers to the degree to which a material can sustain plastic deformation during tensile stress. From these micrographs, with a higher speed and laser power, porosity is larger, and the failure effect occurs at a larger magnitude than the other constant parameters. The failure was caused at the higher speed and power within the graded specimen and tore from there. Some

similarities in tearing and fracture can be seen at the edge of both the MGM and 180W specimens.

3.5 Fatigue Analysis and Results

The stress values for an r-ratio of 0.1 were calculated from the tensile screw-driven machine results and used to perform the fatigue test. The cycle count for each test was 30, due to limited time and machine capabilities. In each of the tests, there is permanent deformation present when compared to the original sample's dimensions (Figure 3.8).

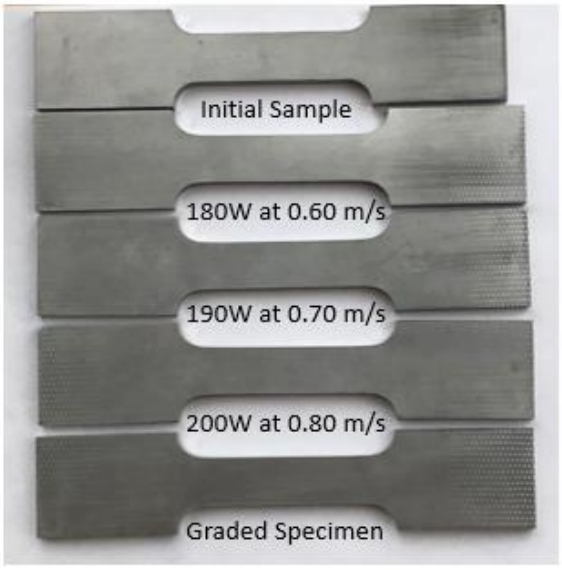

Figure 3.8 Cyclic fatigue response MGM and constant parameter specimens compared to original, where permanent deformation occurs.

The tensile tests on the screw-driven machine were used to set the stress conditions of each of the fatigue tests. The ultimate tensile stress (UTS) was recorded, and the stress ratio was calculated using that value. The stress amplitude of the calculated stress range was calculated as well.

Table 3-3 Loading conditions for stress-controlled fatigue test based on the tensile test results, with r-ratio of 0.1.

Sample	UTS (MPa)	R-Ratio	Max Stress (MPa)	Min Stress (MPa)	Stress Amplitude	Cycle Count
Graded Specimen	618.2	0.1	556.38	61.82	309.1	30
180W, 0.60m/s	617.8	0.1	556.02	61.78	308.9	30
190W, 0.70 m/s	610.2	0.1	549.18	61.02	305.1	30
200W, 0.08 m/s	595.6	0.1	536.04	59.56	297.8	30

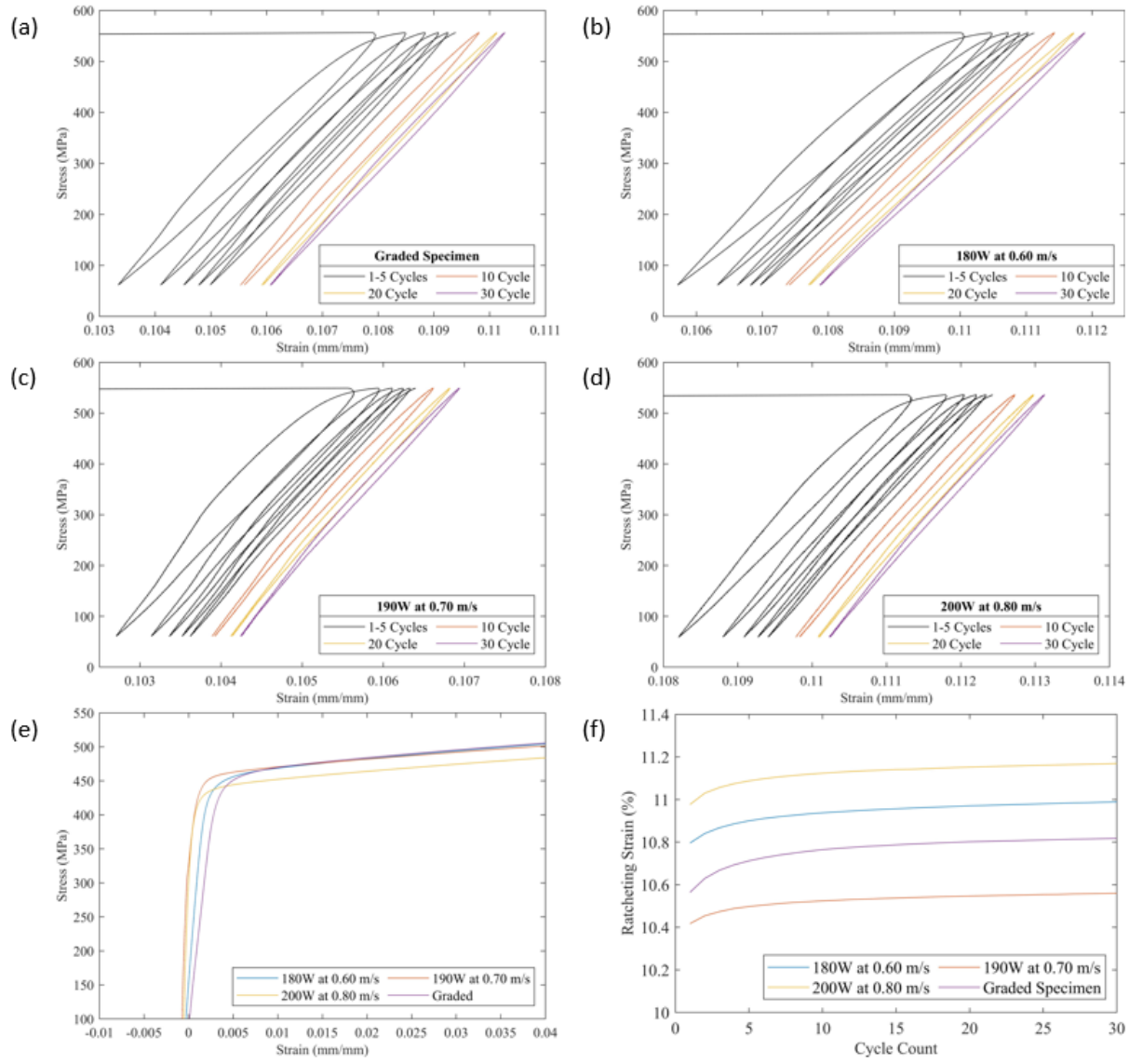

Figure 3.9 (a)graded specimen, (b) 180W at 0.60 m/s, (c) 190W at 0.70 m/s, and (d) 200W at 0.80 m/s. (e) yield location of all four specimens during fatigue test (f) ratcheting strain versus cycle count.

The first five cycles, tenth, twentieth, and thirtieth cycles, are plotted for each tested sample (Figure 3.9a-d). For each loading, the stress-strain plot can be divided into the area under the curve of the loading and unloading regimes [38]. The linear regions that can be seen through each test's cycles are the areas of linear elastic loading and unloading.

The ratcheting strain (Figure 3.9) is dependent on the loading stress level, and due to the variations of the stress ranges used for the LCF tests, there is no trend between each of the samples tested. However, the MGM specimen stabilizes slower than the other specimens, suggesting that the cyclic hardening effect occurs at a slower rate.

Table 3-4 (Table A) Yield stress results from cyclic fatigue and screw driven tensile test of each dog bone specimen. (Table B) Percent difference of constant parameters when compared to MGM specimen, to show yield strength degree is constant parameters.

Table A	**Low Cycle Fatigue Response**		**Screw- Driven Tension Response**	
Specimen	Displacement Rate	Yield Stress (MPa)	Displacement Rate	Yield Stress (MPa)
180W at 0.60 m/s	2 mm/min	449.71	0.1mm/sec	462.43
190W at 0.70 m/s		450.9		452.44
200W at 0.80 m/s		435.3		432.85
MGM Specimen		451.52		466.57

Table B	**Yield Stress (%) LCF Test**	**Yield Stress (%) Tensile Test**
180W at 0.60 m/s	-0.40	-0.89
190W at 0.70 m/s	-0.14	-3.03
200W at 0.80 m/s	-3.59	-7.23
MGM Specimen	0	0

The YS of the fatigue tested specimens were calculated and compared to the YS results from the screw-driven tension test (Table 3-4). As the constant parameters increased, the YS decreased in the tension tests, which was not true in the fatigue test. The MGM specimen performed higher in both tests, and the constant parameter of 200W at 0.80 m/s performed lower than all the tested samples. The deviations in the YS results could result from the range of raw data points chosen to represent the linear elastic region of the test. The results calculated from the LCF test are lower than the tension results except for the 200W at 0.80 m/s parameters, resulting from the displacement rate change between the tests. When comparing

the percent difference of the constant parameter specimens to the graded specimen, each of the constant parameters have a yield strength below the MGM specimen. Overall, the Graded specimen performed according to the initial assumption that the MGM where the microstructure was smaller along the edges would perform better.

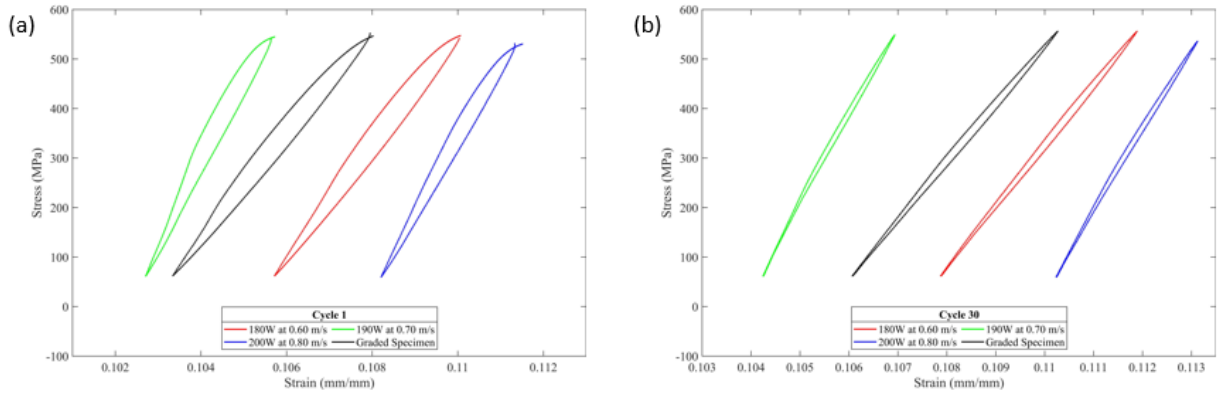

Figure 3.10 Cyclic fatigue results of the graded and constant specimens at (a) cycle one and (b) cycle 30.

To investigate the relation between the cycles of each of the samples tested, the first and last cycles were plotted (Figure 3.10). The hysteresis loops for all tests increase in the strain as the cycle count increase, which results in the accumulation of ratcheting strain. The hysteresis loops' width narrows, which indicates cyclic hardening, which is similar to the material observed by Lu, et al. [36]. The shape of cycle 1 for the MGM and 180W at 0.60 m/s specimens are broader than the remaining specimens. As the cycle count increases, the ratcheting strain rate decreases, which is due to the cyclic hardening effect. As the parameter set changes, there is no trend in the increase or decrease of each cycle's strains. The strain output is dependent on the stress ratio chosen for the parameters, which can be attributed to the change in strain between the specimens. The graded specimen has a higher cyclic hardening effect than 190W at 0.70m/s and 200W at 0.80 m/s parameter sets.

Chapter 4

4. Conclusions and Future Work

4.1 Summary and Conclusions

3D Printing and Characterizing Materials with Gradient Microstructure:

In SLM, multiple process parameters affect the formation of the microstructure, the change in microstructure through the build is known as MGM. Specific process parameters were changed stepwise throughout the build direction. The process parameters include laser power, scanning speed, and hatch spacing due to their ability to be manipulated during the build. Hatch spacing is increased from 75 microns to 115 microns by 10 microns every 2 millimeters; in the build direction, scanning speed was decreased from 0.75 m/s to 0.55 m/s, where the optimized scanning speed is 0.75 m/s, and a constant laser power of 200W. The laser power was decreased from 200W to 180W, and the speed was decreased from 0.80 m/s to 0.60 m/s. This machine's current optimized variable includes a laser power of 200W, scanning speed of 0.75 m/s, and a hatch spacing of approximately 110 microns. Cube samples were built with sides equal to 10 millimeters with the gradation of parameters, and they were polished and etched for imaging. Optical and SEM images were taken to reveal the grain and melt pool characteristics and cellular characteristics, respectively. Image processing was implemented on these images to provide cellular and melt pool characteristics. The melt pool characteristics analyzed were the grain area, melt pool width, area, depth, track-track boundary, layer- layer boundary, and the equiaxial cell area.

As the hatch spacing increased, the optical images showed an increase in the melt pool width and a decrease in the depth, resulting from molten material solidifying with larger

spacing. The epitaxial grain growth decreases as the spacing increases due to a higher temperature gradient. With speed MGMs the grains become more significant due to the higher temperature gradient as speed decreases. The melt pools were deeper with a narrow impression, which is referred to as the keyhole effect. In the power and speed MGM, the specimen was over etched as the speed and power decreased. The grain formation is smaller due to the reduced cooling time as the speed and power are larger. There is no clear visual trend in the melt pools of the optical images. Still, the epitaxial grain growth appears to be halted and shows no clear epitaxial growth in the temperature gradient direction.

In the SEM images, before image analysis, certain characteristics can be seen. There were areas of unconsolidated powder, and the cell boundaries were more detectable in some areas over others. In hatch spacing, this characteristic decreased as the hatch spacing increased.

The image processing analysis showed a linear trend in hatch spacing, where the cell area increased as the hatch spacing increase; however, the trend in the speed cell size was not apparent. As the hatch spacing increased, the standard deviation increased, suggesting that a high hatch spacing may result in varied cell size. When the speed is decreased from 0.70 m/s to 0.55 m/s, the trend shows that the cell area and standard deviation increase. However, the scanning speed of 0.70 m/s is an outlier in the results. As the scanning speed and laser power decreased, the cell area increased faster and began to stabilize. The melt pool size showed linear trends in each of the MGM specimens. As hatch spacing increases and scanning speed decreases, the melt pool area increases. When the laser power and scanning speed is decreased, the melt pool area decreases.

Experimental Analysis of Materials with Graded Microstructure:

The conclusions from Chapter 2 provided the framework for the MGM designed for mechanical analysis. The parameter set with a gradient laser power and scanning speed was chosen due to the higher rate of the cell size change as the parameters changed. The build's goal was to create an MGM where the cell size and melt pool were smaller on the edges and larger in the center. Dog bone samples were printed where the laser power changed from 180W to 200W, and the scanning speed went from 0.60 m/s to 0.80 m/s. Additional dog bones were printed with consistent laser power and scanning speed, and the parameter sets 180W at 0.60 m/s, 190W at 0.70 mm/s, and 200W at 0.80 m/s for comparison. The sample was printed lying flat, where the build direction was parallel through the thickness.

Each of these samples was tension testing using a hydraulic and screw-driven tensile machine. These samples were pulled at a displacement rate of 2mm/min to failure. The extensometer used on the hydraulic machine had a gauge length of 1 inch, and the one used on the screw-driven machine was a 2 in extensometer. The hydraulic tension test strain was measured through the extensometer up to 50% strain, and the reaming strain to failure was calculated based on displacement. The specimens' original gauge length was 55 millimeters, and the uniaxial tension tests failed at approximately 50-57% strain, which is a displacement of 27.5-31.75 millimeters.

The 180W at 0.60 m/s samples performed the best in terms of yield strength and Ultimate Tensile Strength (UTS), where the graded specimen was near these results as well, and the remaining specimens fell below on performance. The largest difference between the

machines in terms of results in the elongation at break. Samples testing using the screw-driven machine failed at a faster strain than the other specimens. The yield strength of these specimens ranged from 432 MPa to 466 MPa, and the UTS ranged from 595 MPa to 619 MPa. It can be concluded from these results that the MGM performed at a higher rate than the parameters that were not on the edges of the sample. The assumption that the MGM would perform higher due to the gradation of process parameters is not accurate with this set of parameters.

The fracture microscopy showed that each of the samples was very ductile. The MGM fractured at the center where the parameter set provided larger microstructural properties. This suggests that fracture in the MGM will result from the more unstable microstructure, but the tensile test reveals this sample was more substantial than the higher speeds and power because the edges were comprised of smaller melt pools and cells.

The specimens were tested for low cycle fatigue with a stress ratio of 0.1 of the UTS. As the parameters decreased, the YS decreased for the tensile tests. However, this was untrue in the fatigue tests, which is most likely due to the strain rate change. The MGM specimen performed higher in both tests, and the constant parameter of 200W at 0.80 m/s performed lower than all of the tested samples. The deviations in the YS results could result from the range of raw data points chosen to represent the linear elastic region of the test.

Overall, the Graded specimen performed according to the initial assumption that the MGM microstructure was smaller along the edges would perform better. The first and last cycles were plotted. The hysteresis loops for all tests increase in the strain as the cycle count increase, which results in the accumulation of ratcheting strain—the width of the hysteresis

loops narrows, which indicates cyclic hardening. The shape of cycle 1 for the MGM and 180W at 0.60 m/s specimens is broader than the remaining specimens. As the cycle count increases, the ratcheting strain rate decreases, which is due to the cyclic hardening effect. As the parameter set changes, there is no trend in the increase or decrease of each cycle's strains.

4.2 Future Work

Cellular Characterization: This work focused on the equiaxial cellular shape characteristics of these graded specimens, which provided an introductory analysis of one component of this material's microstructure. Continued study on elongated cells and the formation of melt pools and grains will give further insight into these materials with graded microstructure produced by SLM. The characterization of these graded samples has provided information that can create a neural model. If a particular cell size is desired, a code can input the area and possibly give output parameters. Further analysis at the boundary and areas where the parameters change should be conducted, along with Electron Back Scatter Diffraction (EBSD) analysis, clearly depicts grain formation.

Experimental Implementation: The cyclic fatigue response should include high cycle fatigue to observe elastic deformation properties in the material. A further examination of low cycle fatigue with a higher cycle count provides additional plastic deformation properties and a basis of comparison for the results outlined in this writing. Once a foundation on these properties is established, there should be further analysis on crack propagation and other experimental procedures.

Numerical Simulation: SLM is one of the preferred AM processes due to its exceptional ability to produce complex structures with the suitable mechanical performance [39]. Material properties can be determined experimentally through static and cyclic material response. Once variables have been defined, theoretical models can be designed to represent this SLM builds' microstructure. The powder will experience melting and solidification at different rates, and due to the laser process, there is heating and cooling that occurs. Thus, investigating the physical aspect during the build can be ambiguous. Numerical simulation is implemented to depict the SLM process parameters' influence on the microstructure and mechanical properties of these intricate structures. This method is used to uncover the complex effects that PBF has on the parts being printed and provides visibility into SLM printed parts. The insight provided from these simulations include processes of physics and control [40]. To study the effect of gradient process parameters on the microstructure, numerical analysis, including finite element and crystal plasticity, is often employed. Crystal Plasticity (CP) modeling is a well-established method for the computational investigation of mechanical properties in crystalline materials [41]. A comparison of experimental and simulated results should be performed to determine if the numerical model can predict the build's mechanical response.

References

[1] S. L. N. Ford, "Additive Manufacturing Technology: Potential Implications for U.S. Manufacturing Competitiveness," *Journal of International Commerce and Economics,* September 24, 2014 2014. [Online]. Available: https://ssrn.com/abstract=2501065.

[2] I. Gibson, D. W. Rosen, and B. Stucker, *Additive Manufacturing Technologies: Rapid Prototyping to Direct Digital Manufacturing*. Springer Publishing Company, Incorporated, 2009.

[3] X. Song, W. Zhai, R. Huang, J. Fu, M. Fu, and F. Li, "Metal-Based 3D-Printed Micro Parts & Structures," in *Reference Module in Materials Science and Materials Engineering*: Elsevier, 2020.

[4] L. Jiao, Z. Chua, S. Moon, J. Song, G. Bi, and H. Zheng, "Femtosecond Laser Produced Hydrophobic Hierarchical Structures on Additive Manufacturing Parts," *Nanomaterials,* vol. 8, p. 601, 08/07 2018, doi: 10.3390/nano8080601.

[5] R. M. Mahamood and E. T. Akinlabi, "Types of Functionally Graded Materials and Their Areas of Application," in *Functionally Graded Materials*, R. M. Mahamood and E. T. Akinlabi Eds. Cham: Springer International Publishing, 2017, pp. 9-21.

[6] M. J. Schneider and M. S. Chatterjee, "Introduction to Surface Hardening of Steels[1]," *vol. 4A, Steel Heat Treating Fundamentals and Processes*: ASM International, 2013, p. 0. [Online]. Available: https://doi.org/10.31399/asm.hb.v04a.a0005771

[7] S. Kurian, "Process-Structure-Property Relationship Study of Selective Laser Melting using Molecular Dynamics," Master of Science, Mechanical Engineering, Virgnia Polytechnic Institute and State University, 2019.

[8] W. M. Tucho, V. H. Lysne, H. Austbø, A. Sjolyst-Kverneland, and V. Hansen, "Investigation of effects of process parameters on microstructure and hardness of SLM manufactured SS316L,"

Journal of Alloys and Compounds, vol. 740, pp. 910-925, 2018/04/05/ 2018, doi: https://doi.org/10.1016/j.jallcom.2018.01.098.

[9] T. Mishurova, K. Artzt, J. Haubrich, G. Requena, and G. Bruno, "New aspects about the search for the most relevant parameters optimizing SLM materials," *Additive Manufacturing,* vol. 25, pp. 325-334, 2019/01/01/ 2019, doi: https://doi.org/10.1016/j.addma.2018.11.023.

[10] D. S. Nguyen, H. S. Park, and C. M. Lee, "Optimization of selective laser melting process parameters for Ti-6Al-4V alloy manufacturing using deep learning," *Journal of Manufacturing Processes,* vol. 55, pp. 230-235, 2020/07/01/ 2020, doi: https://doi.org/10.1016/j.jmapro.2020.04.014.

[11] J. Suryawanshi, K. G. Prashanth, and U. Ramamurty, "Mechanical behavior of selective laser melted 316L stainless steel," *Materials Science and Engineering: A,* vol. 696, pp. 113-121, 2017/06/01/ 2017, doi: https://doi.org/10.1016/j.msea.2017.04.058.

[12] R. Casati, J. Lemke, and M. Vedani, "Microstructure and Fracture Behavior of 316L Austenitic Stainless Steel Produced by Selective Laser Melting," *Journal of Materials Science & Technology,* vol. 32, no. 8, pp. 738-744, 2016/08/01/ 2016, doi: https://doi.org/10.1016/j.jmst.2016.06.016.

[13] J. Yang *et al.*, "Role of molten pool mode on formability, microstructure and mechanical properties of selective laser melted Ti-6Al-4V alloy," *Materials & Design,* vol. 110, pp. 558-570, 2016/11/15/ 2016, doi: https://doi.org/10.1016/j.matdes.2016.08.036.

[14] J. Hlinka *et al.*, "Complex Corrosion Properties of AISI 316L Steel Prepared by 3D Printing Technology for Possible Implant Applications," (in eng), *Materials (Basel),* vol. 13, no. 7, p. 1527, 2020, doi: 10.3390/ma13071527.

[15] L.-C. Zhang, J. Wang, Y. Liu, Z. Jia, and S.-X. Liang, "Additive Manufacturing of Titanium Alloys," in *Reference Module in Materials Science and Materials Engineering*: Elsevier, 2020.

[16] Y.-L. Lo, B.-Y. Liu, and H.-C. Tran, "Optimized hatch space selection in double-scanning track selective laser melting process," *The International Journal of Advanced Manufacturing Technology,* vol. 105, no. 7, pp. 2989-3006, 2019/12/01 2019, doi: 10.1007/s00170-019-04456-w.

[17] Z. Dong, Y. Liu, W.-B. Wen, J. Ge, and J. Liang, "Effect of Hatch Spacing on Melt Pool and As-built Quality During Selective Laser Melting of Stainless Steel: Modeling and Experimental Approaches," *Materials,* vol. 12, p. 50, 12/24 2018, doi: 10.3390/ma12010050.

[18] R. Mertens, S. Clijsters, K. Kempen, and J.-P. Kruth, "Optimization of Scan Strategies in Selective Laser Melting of Aluminum Parts With Downfacing Areas," *Journal of Manufacturing Science and Engineering,* vol. 136, 12/01 2014, doi: 10.1115/1.4028620.

[19] Y. Deng, Z. Mao, N. Yang, X. Niu, and X. Lu, "Collaborative Optimization of Density and Surface Roughness of 316L Stainless Steel in Selective Laser Melting," (in eng), *Materials (Basel),* vol. 13, no. 7, p. 1601, 2020, doi: 10.3390/ma13071601.

[20] I. W. Hamley *et al.*, "Crystallization in Poly(l-lactide)-b-poly(ε-caprolactone) Double Crystalline Diblock Copolymers: A Study Using X-ray Scattering, Differential Scanning Calorimetry, and Polarized Optical Microscopy," *Macromolecules,* vol. 38, no. 2, pp. 463-472, 2005/01/01 2005, doi: 10.1021/ma0481499.

[21] H. Yeung, Z. Yang, and L. Yan, "A meltpool prediction based scan strategy for powder bed fusion additive manufacturing," *Additive Manufacturing,* vol. 35, p. 101383, 2020/10/01/ 2020, doi: https://doi.org/10.1016/j.addma.2020.101383.

[22] J. Akram, P. Chalavadi, D. Pal, and B. Stucker, "Understanding grain evolution in additive manufacturing through modeling," *Additive Manufacturing,* vol. 21, pp. 255-268, 2018/05/01/ 2018, doi: https://doi.org/10.1016/j.addma.2018.03.021.

[23] F. Yan, W. Xiong, and E. Faierson, "Grain Structure Control of Additively Manufactured Metallic Materials," *Materials,* vol. 10, p. 1260, 11/02 2017, doi: 10.3390/ma10111260.

[24] N. Chatterjee, K. Andresen, M. Thomas, L. Pollack, and E. Kirkland, "A Simple Method for Imaging DNA using SEM," *Microscopy Today,* vol. 16, no. 2, pp. 38-39, 2008, doi: 10.1017/S1551929500055917.

[25] R. Schmitt, "Scanning Electron Microscope," in *CIRP Encyclopedia of Production Engineering*, L. Laperrière and G. Reinhart Eds. Berlin, Heidelberg: Springer Berlin Heidelberg, 2014, pp. 1085-1089.

[26] C. A. Schneider, W. S. Rasband, and K. W. Eliceiri, "NIH Image to ImageJ: 25 years of image analysis," *Nature Methods,* vol. 9, no. 7, pp. 671-675, 2012/07/01 2012, doi: 10.1038/nmeth.2089.

[27] B. Barkia *et al.*, "On the origin of the high tensile strength and ductility of additively manufactured 316L stainless steel: Multiscale investigation," *Journal of Materials Science & Technology,* vol. 41, 11/01 2019, doi: 10.1016/j.jmst.2019.09.017.

[28] W. Shifeng, L. Shuai, W. Qingsong, C. Yan, Z. Sheng, and S. Yusheng, "Effect of molten pool boundaries on the mechanical properties of selective laser melting parts," *Journal of Materials Processing Technology,* vol. 214, no. 11, pp. 2660-2667, 2014/11/01/ 2014, doi: https://doi.org/10.1016/j.jmatprotec.2014.06.002.

[29] G. Jing, W. Huang, H. Yang, and Z. Wang, "Microstructural evolution and mechanical properties of 300M steel produced by low and high power selective laser melting," *Journal of Materials Science & Technology,* vol. 48, pp. 44-56, 2020/07/01/ 2020, doi: https://doi.org/10.1016/j.jmst.2019.12.020.

[30] M. Simonelli *et al.*, "A Study on the Laser Spatter and the Oxidation Reactions During Selective Laser Melting of 316L Stainless Steel, Al-Si10-Mg, and Ti-6Al-4V," *Metallurgical and Materials*

Transactions A, vol. 46, no. 9, pp. 3842-3851, 2015/09/01 2015, doi: 10.1007/s11661-015-2882-8.

[31] A. Bauereiß, T. Scharowsky, and C. Körner, "Defect generation and propagation mechanism during additive manufacturing by selective beam melting," *Journal of Materials Processing Technology,* vol. 214, no. 11, pp. 2522-2528, 2014/11/01/ 2014, doi: https://doi.org/10.1016/j.jmatprotec.2014.05.002.

[32] N. Aboulkhair, N. Everitt, I. Ashcroft, and C. Tuck, "Reducing Porosity in AlSi10Mg Parts Processed by Selective Laser Melting," *Additive Manufacturing,* vol. 1-4, 08/01 2014, doi: 10.1016/j.addma.2014.08.001.

[33] C. Han *et al.*, "Titanium/hydroxyapatite (Ti/HA) gradient materials with quasi-continuous ratios fabricated by SLM: Material interface and fracture toughness," *Materials & Design,* vol. 141, pp. 256-266, 2018/03/05/ 2018, doi: https://doi.org/10.1016/j.matdes.2017.12.037.

[34] Y.-J. Liang, D. Liu, and H.-M. Wang, "Microstructure and mechanical behavior of commercial purity Ti/Ti–6Al–2Zr–1Mo–1V structurally graded material fabricated by laser additive manufacturing," *Scripta Materialia,* vol. 74, pp. 80-83, 2014/03/01/ 2014, doi: https://doi.org/10.1016/j.scriptamat.2013.11.002.

[35] B. Chen, Y. Su, Z. Xie, C. Tan, and J. Feng, "Development and characterization of 316L/Inconel625 functionally graded material fabricated by laser direct metal deposition," *Optics & Laser Technology,* vol. 123, p. 105916, 2020/03/01/ 2020, doi: https://doi.org/10.1016/j.optlastec.2019.105916.

[36] X. Lu *et al.*, "Cyclic plasticity of an interstitial high-entropy alloy: experiments, crystal plasticity modeling, and simulations," *Journal of the Mechanics and Physics of Solids,* vol. 142, p. 103971, 2020/09/01/ 2020, doi: https://doi.org/10.1016/j.jmps.2020.103971.

[37] A. Vinogradov, I. S. Yasnikov, H. Matsuyama, M. Uchida, Y. Kaneko, and Y. Estrin, "Controlling strength and ductility: Dislocation-based model of necking instability and its verification for ultrafine grain 316L steel," *Acta Materialia,* vol. 106, pp. 295-303, 2016/03/01/ 2016, doi: https://doi.org/10.1016/j.actamat.2016.01.005.

[38] H. Yun and M. Modarres, "Measures of Entropy to Characterize Fatigue Damage in Metallic Materials," *Entropy,* vol. 21, p. 804, 08/17 2019, doi: 10.3390/e21080804.

[39] M. Galati and L. Iuliano, "A literature review of powder-based electron beam melting focusing on numerical simulations," *Additive Manufacturing,* vol. 19, pp. 1-20, 2018/01/01/ 2018, doi: https://doi.org/10.1016/j.addma.2017.11.001.

[40] A. Razavykia, E. Brusa, C. Delprete, and R. Yavari, "An Overview of Additive Manufacturing Technologies-A Review to Technical Synthesis in Numerical Study of Selective Laser Melting," (in eng), *Materials (Basel),* vol. 13, no. 17, p. 3895, 2020, doi: 10.3390/ma13173895.

[41] F. Roters, P. Eisenlohr, T. Bieler, and D. Raabe, *Crystal Plasticity Finite Element Methods*. 2010.

Appendix

Appendix A: MGM Melt Pool and Cell Area Characteristics

Parameter Set	Power	Speed	Hatch Spacing	Mean Cell Area (µm²)	Average MP Area (mm²)	Average MP Width (mm)	Average MP Depth (mm)	Track-Track Boundary (mm)	Layer-Layer Boundary (mm)	Average Grain Size (µm²)
1	200 W	0.75 m/s	75 µm	0.2074	0.0093	0.2075	0.0802	0.04879	0.20545	462.9185
2	200 W	0.75 m/s	85 µm	0.242	0.0116	0.2069	0.0711	0.04849	0.22563	939.3068
3	200 W	0.75 m/s	95 µm	0.26375	0.0142	0.2319	0.0873	0.04019	0.2468	1131.821
4	200 W	0.75 m/s	105 µm	0.3142	0.0146	0.2602	0.0936	0.04941	0.26452	833.225
5	200 W	0.75 m/s	115 µm	0.3308	0.0175	0.2583	0.0888	0.04317	0.26701	1048.515
6	200 W	0.75 m/s	110 µm	0.2892	0.00534	0.12237	0.05851	0.04163	0.1773	660.0053
7	200 W	0.70 m/s	110 µm	0.2198	0.00925	0.16087	0.08696	0.03747	0.21378	416.2432
8	200 W	0.65 m/s	110 µm	0.25	0.01308	0.17183	0.11821	0.0448	0.22769	506.1961
9	200 W	0.60 m/s	110 µm	0.3402	0.01291	0.1673	0.11884	0.04271	0.24845	641.8768
10	200 W	0.55 m/s	110 µm	0.416	0.01381	0.15616	0.12754	0.04427	0.20724	851.5881
11	200 W	0.80 m/s	110 µm	0.4076	0.01628	0.21214	0.11422	0.04118	0.14961	413.54461
12	195 W	0.75 m/s	110 µm	0.29833	0.01571	0.17165	0.10027	0.03399	0.14904	473.35761
13	190 W	0.70 m/s	110 µm	0.2715	0.01197	0.18605	0.09774	0.03553	0.17014	480.97735
14	185 W	0.65 m/s	110 µm	0.1995	0.01137	0.20471	0.11784	0.04357	0.15083	540.83448
15	180 W	0.60 m/s	110 µm	0.187	0.01171	0.21168	0.07853	0.0394	0.18199	474.6326

Appendix B: Fracture Micrographs